HHS Public Access

Author manuscript

Cell Stem Cell. Author manuscript; available in PMC 2024 May 06.

Published in final edited form as:

Cell Stem Cell. 2022 April 07; 29(4): 559–576.e7. doi:10.1016/j.stem.2022.02.011.

PPARdelta activation induces metabolic and contractile maturation of human pluripotent stem-cell-derived cardiomyocytes

Nadeera M. Wickramasinghe[1,2,3], **David Sachs**[4,14], **Bhavana Shewale**[1,2,3,14], **David M. Gonzalez**[1,2,3,14], **Priyanka Dhanan-Krishnan**[5], **Denis Torre**[5], **Elizabeth LaMarca**[6,7], **Serena Raimo**[8], **Rafael Dariolli**[5], **Madhavika N. Serasinghe**[9], **Joshua Mayourian**[4], **Robert Sebra**[10], **Kristin Beaumont**[10], **Srinivas Iyengar**[5,11], **Deborah L. French**[8], **Arne Hansen**[12], **Thomas Eschenhagen**[12], **Jerry E. Chipuk**[9], **Eric A. Sobie**[5], **Adam Jacobs**[13], **Schahram Akbarian**[6,7], **Harry Ischiropoulos**[8], **Avi Ma'ayan**[5], **Sander M. Houten**[10], **Kevin Costa**[4], **Nicole C. Dubois**[1,2,15,*]

[1]Department of Cell, Developmental and Regenerative Biology, Icahn School of Medicine at Mount Sinai, New York, NY 10029, USA

[2]Mindich Child Health and Development Institute, Icahn School of Medicine at Mount Sinai, New York, NY 10029, USA

[3]Black Family Stem Cell Institute, Icahn School of Medicine at Mount Sinai, New York, NY 10029, USA

[4]Department of Medicine, Icahn School of Medicine at Mount Sinai, New York, NY 10029, USA

[5]Department of Pharmacological Sciences, Icahn School of Medicine at Mount Sinai, New York, NY 10029, USA

[6]Friedman Brain Institute, Icahn School of Medicine at Mount Sinai, New York, NY 10029, USA

[7]Department of Psychiatry, Icahn School of Medicine at Mount Sinai, New York, NY 10029, USA

[8]Children's Hospital of Philadelphia Research Institute, Philadelphia, PA, USA

[*]Correspondence: nicole.dubois@mssm.edu.

AUTHOR CONTRIBUTIONS

N.M.W. and N.C.D. designed and performed experiments and analyzed data. D.S., D.T., A.M., and K.C. analyzed RNA-seq and ATAC-seq data. D.M.G., B.S., P.D.-K., E.L., S.R., R.D., M.N.S., R.S., K.B., S.I., J.M., J.E.C., E.A.S., H.I., and S.A. performed experiments and data analysis. A.H. and T.E. shared expertise and materials for generating EHTs from hPSC-CMs. N.M.W. and N.C.D. wrote the manuscript with input from all authors.

SUPPLEMENTAL INFORMATION

Supplemental information can be found online at https://doi.org/10.1016/j.stem.2022.02.011.

DECLARATION OF INTERESTS

The authors declare no competing interest.

INCLUSION AND DIVERSITY

We worked to ensure diversity in experimental samples through the selection of the cell lines. One or more of the authors of this paper self-identifies as a member of the LGBTQ+ community. One or more of the authors of this paper received support from a program designed to increase minority representation in science. While citing references scientifically relevant for this work, we also actively worked to promote gender balance in our reference list.

ADDITIONAL RESOURCES

RNAseq data can be searched in the publicly accessible RNASeq Resource Website (amp.pharm.mssm.edu/dubois/).

[9]Department of Oncological Sciences, Icahn School of Medicine at Mount Sinai, New York, NY 10029, USA

[10]Department of Genetics and Genomic Sciences, Icahn School of Medicine at Mount Sinai, New York, NY 10029, USA

[11]Mount Sinai Institute for Systems Biomedicine, Icahn School of Medicine at Mount Sinai, New York, NY 10029, USA

[12]University Medical Center Hamburg-Eppendorf, Hamburg 20246, Germany

[13]Department of Obstetrics and Gynecology, Icahn School of Medicine at Mount Sinai, New York, NY 10029, USA

[14]These authors contributed equally

[15]Lead contact

SUMMARY

Pluripotent stem-cell-derived cardiomyocytes (PSC-CMs) provide an unprecedented opportunity to study human heart development and disease, but they are functionally and structurally immature. Here, we induce efficient human PSC-CM (hPSC-CM) maturation through metabolic-pathway modulations. Specifically, we find that peroxisome-proliferator-associated receptor (PPAR) signaling regulates glycolysis and fatty acid oxidation (FAO) in an isoform-specific manner. While PPARalpha (PPARa) is the most active isoform in hPSC-CMs, PPARdelta (PPARd) activation efficiently upregulates the gene regulatory networks underlying FAO, increases mitochondrial and peroxisome content, enhances mitochondrial cristae formation, and augments FAO flux. PPARd activation further increases binucleation, enhances myofibril organization, and improves contractility. Transient lactate exposure, which is frequently used for hPSC-CM purification, induces an independent cardiac maturation program but, when combined with PPARd activation, still enhances oxidative metabolism. In summary, we investigate multiple metabolic modifications in hPSC-CMs and identify a role for PPARd signaling in inducing the metabolic switch from glycolysis to FAO in hPSC-CMs.

Graphical abstract

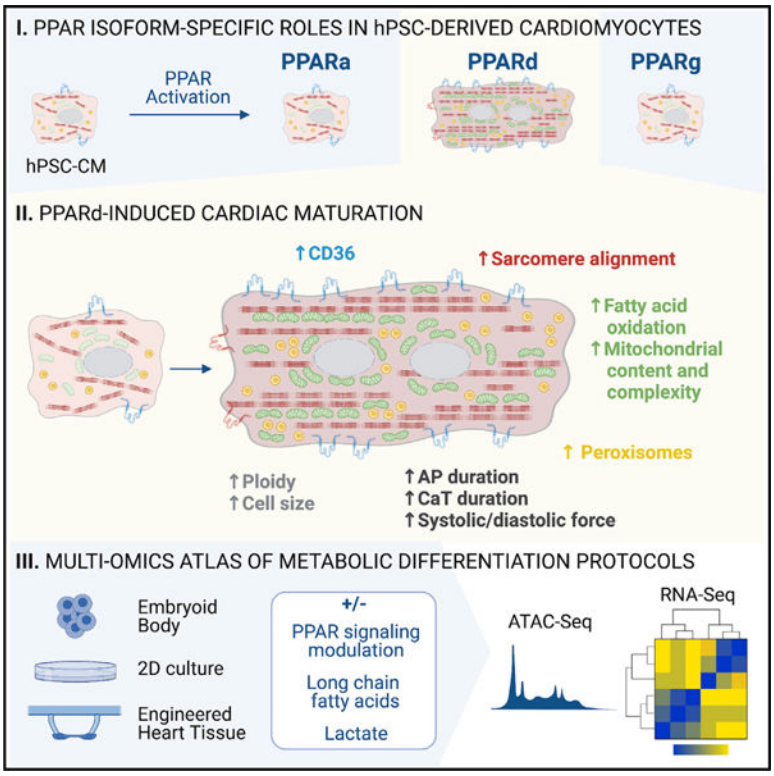

In brief

Efficient maturation of *in vitro*-generated cells remains a challenge and the underlying mechanisms are poorly understood. Here Wickramasinghe and colleagues show that PPAR signaling acts in an isoform-specific manner to enhance metabolic and electrophysiological maturation of pluripotent stem-cell-derived cardiomyocytes.

INTRODUCTION

The differentiation of human pluripotent stem cells (hPSCs) into various cell types provides unprecedented opportunities to study human cells and tissues *in vitro*. This is particularly relevant for the heart, as heart disease remains a leading cause of death, but access to tissue samples and relevant animal models remains challenging (Brandão et al., 2017; Hasenfuss, 1998; Houser et al., 2012; Tsang et al., 2016; Virani et al., 2020). Human PSC-derived cardiomyocytes (hPSC-CMs) can be derived with high efficiency and have been successfully used for disease modeling, regenerative therapies, and drug discovery (Burridge et al., 2015; Kattman et al., 2011; Lian et al., 2012, 2013; Murry and Keller, 2008; Yang et al., 2008; Zhang et al., 2012). However, hPSC-CMs remain immature, as assayed by their cell morphology, gene expression, electrophysiological properties, mitochondrial content, metabolic activity, contractile force, and the absence of T-tubules, which limits their therapeutic and research potential (van den Berg et al., 2015; DeLaughter et al., 2016; Gherghiceanu et al., 2011; Karbassi et al., 2020; Liu et al., 2010; Parikh et al., 2017; Thavandiran et al., 2013; Ulmer and Eschenhagen, 2020; Yang et al., 2014a). Current hPSC-CM differentiation protocols are largely based on recapitulating the developmental

sequential stages of *in vivo* heart development; we hypothesize that hPSC-CM immaturity is the result of an incomplete recapitulation of such processes *in vitro* (Calderon et al., 2016; Kattman et al., 2011; Lian et al., 2012, 2013; Yang et al., 2008).

Cardiac maturation involves coordinated metabolic, electrochemical, mechanical, and cell-cell interaction mechanisms. Consequently, strategies to enhance hPSC-CM maturation have focused on long-term cultures (DeLaughter et al., 2016; Kamakura et al., 2013), tissue engineering (Correia et al., 2018; Giacomelli et al., 2020; Lee et al., 2017b; Leonard et al., 2018; Li et al., 2018; Lopez et al., 2021; Nunes et al., 2013; Serpooshan et al., 2017; Shadrin et al., 2017; Thavandiran et al., 2013; Tiburcy et al., 2017; Zhao et al., 2020), electrical stimulation (Nunes et al., 2013; Ronaldson-Bouchard et al., 2018), activation of signaling pathways (Buikema et al., 2020; Gentillon et al., 2019; Kosmidis et al., 2015; Lopez et al., 2021; Murphy et al., 2021; Parikh et al., 2017; Poon et al., 2015; Yang et al., 2014b), and epigenetic modifications and substrate utilization (Correia et al., 2017; Feyen et al., 2020; Hu et al., 2018; Mills et al., 2017; Nakano et al., 2017; Yang et al., 2019). While many of these approaches successfully enhance hPSC-CM maturation, strategies to generate adult-like CMs are still lacking and are likely driven by a combination of the aforementioned parameters.

In addition to the complex morphological and structural changes that occur as the heart grows, the embryo also encounters systemic changes, such as the well-characterized metabolic switch (Ascuitto and Ross-Ascuitto, 1996; Lopaschuk and Jaswal, 2010; Piquereau and Ventura-Clapier, 2018). The adult heart predominantly utilizes mitochondrial fatty acid oxidation (FAO) to fuel ATP production (Houten et al., 2016; Stanley et al., 2005). In contrast, the developing heart utilizes anaerobic glycolysis and lactate oxidation (Lopaschuk and Jaswal, 2010; Piquereau and Ventura-Clapier, 2018). The metabolic switch allows the organism to meet the higher energy demands of the growing heart as FAO generates more ATP per mole of substrate oxidized than any other pathway (Lopaschuk and Jaswal, 2010; Piquereau and Ventura-Clapier, 2018).

Although a marked metabolic shift toward FAO occurs postnatally, the transcriptional program required for FAO is established as early as midgestation (Menendez-Montes et al., 2016; Uosaki et al., 2015; DeLaughter et al., 2016). The heart begins to express genes involved in FAO pathways at midgestation. For example, the peroxisome-proliferator-associated receptor (PPAR) pathway turns on at midgestation and increases continuously to remain active throughout adulthood. PPARs belong to a class of ligand-activated transcription factors (nuclear hormone receptors), which are involved in growth, proliferation, and metabolism, and which exist in three isoforms: PPARalpha (PPARa), PPARbeta/delta (PPARd), and PPARgamma (PPARg) (Ahmadian et al., 2013; Barger and Kelly, 2000; Houten et al., 2016; Lopaschuk and Jaswal, 2010). Knockout (KO) mouse models for PPARa and PPARd have underscored their role in metabolic regulation. PPARa-deficient mice show reduced FAO, but fasting is required for this phenotype to become apparent (Liu et al., 2011). Deletion of PPARd is embryonically lethal; however, CM-restricted PPARd KO mice are viable with reduced FAO and increased glucose uptake in adulthood (Barak et al., 2002; Cheng et al., 2004). Based on these findings, we hypothesized

that inducing PPAR signaling *in vitro* would model its contribution to the metabolic switch observed during heart development.

The goal of this study was to recapitulate in hPSC-CMs the metabolic changes that occur during *in vivo* heart development. Together, our findings enable further refinement of differentiation protocols, in an easy and scalable manner, to ultimately yield physiologically relevant cardiac tissue for *in vitro* studies and therapeutics development.

RESULTS

PPAR activation enhances myofibril organization in hPSC-CMs in an isoform-specific manner

To assess PPAR signaling activity during hPSC differentiation, we performed qPCR analysis for the PPAR isoforms, PPARa (*PPARA*), PPARd (*PPARD*), and PPARg (*PPARG*). PPAR gene expression of all isoforms increased during differentiation but remained low relative to 20-week-old fetal and adult heart tissue (Figure 1A). Immunofluorescence (IF) analysis of 16-week-old human fetal heart and hPSC-CMs confirmed the gene expression analysis and reflects PPAR isoform distribution described in the developing mouse heart (Figures 1B, S1A, and S1B; Uosaki et al., 2015). To explore the requirement for PPAR signaling during cardiac differentiation, we used highly selective antagonists to inhibit each PPAR isoform: PPARa: GW6471, PPARd: GSK0660 (Shearer et al., 2008), and PPARg: GW9662. PPAR signaling abrogation throughout differentiation, either individually or in combination, did not affect the generation of hPSCCMs, as measured by the percentage of SIRPA+CD90− cells at day 20 of differentiation (Figures 1C and 1F). However, the combination of all antagonists reduced the total number of cells, suggesting that PPAR signaling is not required for CM specification but may affect cell survival or expansion during early development (Figure 1G). Next, we inhibited PPAR at later stages of CM differentiation, when PPAR expression levels are higher. hPSC-CMs were plated as 2D monolayers at day 20 of differentiation, followed by 2 weeks of PPAR antagonist treatment. Flow cytometry analysis for SIRPA+CD90+ cells showed no difference in hPSC-CM maintenance after PPAR inhibition (Figures 1D and 1H). However, joint inhibition of all three PPAR isoforms resulted in decreased ACTN2 levels (Figures 1E, 1I, and 1J). IF analysis for ACTN2 and cardiac troponin T (cTnT) further illustrated that inhibition of PPARa and of all PPAR isoforms combined resulted in fewer and less organized myofibrils (Figure 1K). Inhibition of PPARd or PPARg did not impact hPSC-CM morphology. To understand whether these isoform-specific effects correlated with the overall abundance of individual PPARs, we performed single-cell RNA sequencing (scRNA-seq) of hPSC-CMs. As expected, we found PPARs to be expressed primarily in hPSC-CMs and not in fibroblasts (Figures 1L and 1M). *PPARA* was the most abundantly expressed isoform, followed by *PPARD* and *PPARG* (Figures 1M and 1N). Lastly, we confirmed expression of PPAR signaling co-activators (*PPARGC1A* and *PPARGC1B*) and the PPAR heterodimer-binding partners retinoid X receptors (*RXRA*, *RXRB*, and *RXRC*), confirming that the PPAR signaling machinery is present in hPSC-CMs and that PPARa is the predominant isoform (Figures S1D–S1F).

To test the effect of PPAR-signaling activation, we treated differentiated hPSC-CMs with isoform-specific small molecule agonists (PPARa: WY14643, PPARd: GW0742 [Sznaidman

et al., 2003], and PPARg: rosiglitazone) for 4 weeks (Figure 2A). IF analysis of cTnT revealed an isoform-specific effect on myofibril alignment in hPSC-CMs treated with GW0742 (PPARd), but not WY14643 (PPARa) or rosiglitazone (PPARg) (Figure 2B). We used MatFiber, a vector-based program, to quantify myofibril organization from cTnT IF images (Figure S2A) (Fomovsky and Holmes, 2010). Myofibrils of PPARd-activated hPSC-CMs, but not PPARa or PPARg, exhibited greater alignment against each other and along the length of the cell and a reduced circularity standard deviation, both of which are characteristic of enhanced CM structural maturation (Figures 2C and 2D). PPARd activation did not affect sarcomere lengths or regularity (Figures S2B and S2C). To assess the effect of PPAR signaling on hPSC-CM proliferation, we performed EdU incorporation assays. The percentage of EdU-positive cells was unchanged in all conditions, suggesting that proliferation is not altered by the activation or inhibition of PPAR signaling in hPSC-CMs (Figure S2D). We measured the surface area of ACTN2+ hPSC-CMs 4 weeks after PPAR treatment, and consistent with increasing cell size during development, activation of PPARd, but not of PPARa or PPARg, increased cell size as well as the number of binucleated hPSC-CMs (Figures 2E and 2F). Together, our data show that PPAR signaling is not required for early cardiac specification. However, PPAR signaling in hPSC-CMs acts in an isoform-specific manner in which PPARd activation enhances sarcomere alignment, increases cell size, and increases numbers of binucleated cells.

PPARd signaling induces the FAO transcriptional program

To investigate the underlying mechanism of PPAR-mediated effects on hPSC-CMs, we performed RNA-seq. In addition to the PPAR-isoform-specific small molecules, we added BSA-complexed long-chain fatty acids (LCFAs) (palmitic acid, oleic acid, and linoleic acid) to address the effects of PPAR activation in the presence and absence of LCFAs. PPAR signaling was induced or inhibited as shown in Figure 2A and SIRPA+CD90− hPSC-CMs were fluorescence-activated cell sorting (FACS) purified 4 weeks after treatment for RNA-seq (Dubois et al., 2011; Elliott et al., 2011; Skelton et al., 2014). Using a cutoff of $p < 0.05$, we identified the highest number of differentially expressed genes relative to control in GW0742-treated (130 upregulated and 66 downregulated), LCFA + GW0742-treated (129 upregulated and 67 downregulated), and GSK0660-treated hPSC-CMs (107 upregulated and 109 downregulated), and a smaller number of differentially expressed genes in all of the other conditions (Figure S3A). KEGG pathway analysis revealed upregulation of metabolism-related terms including ‘‘FA metabolism,’’ ‘‘adipocytokine-signaling pathway,’’ and ‘‘peroxisomes’’ in PPARd-activated hPSC-CMs (Figure 3A). Accordingly, PPARd signaling inhibition resulted in decreased expression of genes associated with the same KEGG pathways. Studies in both the mouse and PSC differentiations have found Wnt signaling to be decreased during cardiac maturation (Buikema et al., 2020; Karakikes et al., 2014; Naito et al., 2006; Ueno et al., 2007; Uosaki et al., 2015). In line with this, PPARd activation resulted in a decrease of Wnt components and an increase of Wnt inhibitors (Figures 3A and 3B). We did not observe large changes in expression of sarcomere genes, cardiac conduction, calcium signaling components, or cardiac transcription factors after PPARd activation (Figure S3B). However, PPARd activation upregulated many genes involved in FAO. These include transporters such as *CD36*, which encodes the primary LCFA plasma membrane transporter and *CPT1A/CPT1B*, coding for carnitine

palmitoyltransferase I (CPT1), which controls the rate-limiting step for the shuttle of LCFA-acyl-carnitines across the outer mitochondrial membrane (Figure 3B). They further include *ACADVL*, the enzyme that catalyzes the first step in LCFA β-oxidation and *HADHA* and *HADHB*, which catalyze the last three reactions in mitochondrial FAO (Figure 3B). Interestingly, *PDK4* was strongly upregulated by PPARd activation. PDK4 inhibits glycolysis-dependent oxidative phosphorylation (OXPHOS) through the inactivation of pyruvate dehydrogenase, which has been demonstrated to be critical for cardiac maturation both *in vivo* and *in vitro* (Nakano et al., 2017). Additional candidates include *ACSL1*, which is involved in forming acyl-LCFAs; *MLYCD*, which catalyzes the conversion of malonyl-CoA to acetyl-CoA; and *ANGPTL4*, which is involved in lipoprotein lipase inhibition and triglyceride clearance, as well as the additional critical FAO enzymes *HMGCS2, ACAA2*, and *ECH1* (Figure 3B). Previous work has suggested that the addition of LCFAs alone could enhance FAO in hPSC-CMs (Yang et al., 2019). We also observed enhanced expression of FAO genes 4 weeks after LCFAs supplementation (*CPT1A*: p = 3.42E−1; *ACADVL*: p = 5.30E−1, and PDK4: p = 3.48E−1); however, this increase was lower than the combination of LCFAs with PPARd signaling activation. To assess whether PPARd signaling is essential for induction of the FAO transcriptional program in hPSC-CMs, we analyzed gene expression after PPARd inhibition. Several of the key regulators (*CD36, CPT1A, ASCL1, CPT1B, HADHA, HADHB*, and *PDK4*) indeed showed significantly decreased expression compared to control hPSC-CMs, suggesting some endogenous activity of PPARd signaling in control conditions. These data are publicly accessible as a searchable project resource (https://maayanlab.cloud/dubois/).

In summary, we show that the PPAR transcription factors act in an isoform-specific manner to activate gene regulatory networks involved in FAO, while simultaneously inhibiting glucose-dependent energy metabolism. We further demonstrate that the inhibition of PPARd results in inverse changes of gene expression, thus suggesting a direct role for PPARd signaling in regulating metabolic pathways in hPSC-CMs.

PPARd activation results in sequential changes in gene expression in hPSC-CMs

We next leveraged existing gene expression datasets comparing day 27 hPSC-CMs to the adult human heart (HH) to explore the hypothesis that PPARd signaling activation drives hPSC-CMs along a developmentally relevant trajectory (Pavlovic et al., 2018). We compared the upregulated and downregulated genes (which are indicative of enhanced or decreased maturation, respectively) from this comparison to the differentially expressed genes after PPARd perturbations. LCFA + GW0742 treatment was the only condition for which the differentially expressed genes exhibited a significant correlation with the genes that were upregulated (p = 6.52E−11) or downregulated (p = 3.19E−4) in comparison with the mature heart tissue (Figure 3C). This unbiased analysis suggests that PPARd activation induces a gene expression profile that more closely correlates with mature CMs compared with any other culture condition tested.

Next, we investigated the temporal mechanisms by which PPARd activation induces FAO in hPSC-CMs by identifying genes regulated shortly after PPARd activation or inhibition and genes differentially expressed over time. We FACS-isolated hPSC-CMs that had been treated

for 1, 2, 3, and 7 days or 4 weeks and performed RNA-seq analysis (Figure 3D). Expression analysis at the different time points identified genes differentially regulated at distinct times during PPARd induction. These groups were (1) genes that were only changed during the first 7 days of treatment (early regulation, 695 upregulated and 1,160 downregulated); (2) genes that remained differentially expressed throughout the treatment timeline (continued regulation, 13 upregulated and 33 downregulated); and (3) genes that were differentially regulated only at the end of the 4-week treatment (late regulation, 39 upregulated and 44 downregulated) (Figure 3E). Within all three subsets, we identified candidates involved in various aspects of heart development (Table S1). To perform pathway analysis, we collated the KEGG pathways identified from both up- and downregulated genes at all time points (Table S2). The genes within the early, continued, and late response groups were compared with the list of KEGG pathways and were extracted if there was a match. This match would indicate that the gene was a component of the listed KEGG pathway and allowed for the investigation of the changing pathways despite the small number of genes in the continued and late response groups (Figures 3E and S3C). As expected, the early response to PPARd activation showed the greatest effect on differentially regulated pathways. For example, there was early upregulation of cell-cycle and OXPHOS genes. Additionally, *PPARA* was downregulated, suggesting that PPARd activation may directly regulate the expression of the other PPAR isoforms. There was also an early downregulation in genes related to glycolysis, galactose metabolism, and the pentose-phosphate pathway. Interesting early candidates included *PFKM*, which catalyzes the rate-limiting step of glycolysis, and *PEX2*, which is a peroxisomal biogenesis factor (Shimozawa et al., 1992; Vora et al., 1980). Continuously upregulated genes included *SLC25A20*, which is involved in the transport of acyl-carnitines into the mitochondrial matrix, and *MLYCD*, a positive regulator of FAO. Within late response genes we identified candidates such as *HADHA* and *HADHB*, which catalyze the last three reactions in mitochondrial FAO (Figure S3C).

Given this dynamic temporal gene expression pattern, we next asked whether transient PPARd activation was sufficient to induce permanent gene expression changes in hPSC-CMs. We induced PPARd signaling for 7 days, continued the culture for an additional 21 days (7-day pulse), and performed RNA-seq analysis. The comparison of the differentially expressed genes in the 7-day pulse with those after 7 or 28 days of continued PPARd activation confirmed a temporal dynamic after PPARd induction (Figure 3F; Table S3). We identified many genes shared between the 7-day pulse and the 7 and 28 days of continuous induction (156 upregulated genes and 9 downregulated genes), demonstrating that a large number of PPARd targets remain differentially expressed even in the absence of continued pathway activation. However, numerous differentially regulated genes did segregate according to the duration of PPARd induction, suggesting that PPARd signaling duration impacts the extent of transformation, with the long-term induction (4 weeks) leading to the most distinct gene expression changes.

Lastly, we investigated PPARd-mediated epigenetic regulation through ATAC-seq. We observed a segregation between control and PPARd-activated hPSC-CMs through principal component analysis (PCA) (Figure S3D), indicating that PPARd activation results in changes to chromatin accessibility in hPSC-CMs. We did not observe significant differences in the overall quantities of promoter- and enhancer-associated peaks (Figure 3G). We

performed differential peak analysis to identify promoter- or enhancer-associated peaks with the biggest increases and decreases in chromatin accessibility in GW0742 compared with control hPSC-CMs (Figure 3H). We showed that PPARd activation enriched a group of genes that were shared in the LCFA + GW0742 condition. This indicates that while the proportions of chromatin accessibility were unchanged, the genes that were affected were unique to PPARd signaling activation, such as, for example, an increase in the chromatin accessibility upstream of *PDK4* (Figure 3I). Some genes that showed differential chromatin accessibility in enhancer regions had been previously linked to cardiac function and disease. *DYSF* and *KCNT2* both had increased chromatic accessibility, where the former encodes a Ca^{2+} sensor involved in maintaining muscle integrity and the latter encodes an outward rectifying K^+ channel (Figures 3I and S3E) (Bhattacharjee et al., 2003; Han et al., 2007). Within the genes with reduced chromatic accessibility, we identified several that were associated with cardiomyopathies (Figures 3I and S3E). An increase in *NIPSNAP3B* is associated with cardiac fibrosis in mice, and *PXDNL* is increased in failing myocardium (Péterfi et al., 2014; Xu et al., 2021). Decreased accessibility of these genes may suggest that PPARd activation promotes healthy myocardium and supports improved cardiac function.

In conclusion, PPARd activation in hPSC-CMs results in a transcriptional and epigenetic profile that more closely resembles that of mature heart tissue. PPARd acts by sequentially activating gene regulatory networks involved in the establishment of FAO, and transient PPARd activation is able to induce permanent changes the same gene regulatory networks, albeit not to the same extent as continuous activation.

PPARd activation increases *in vitro* LCFA uptake and processing

To determine if PPARd activation augments FAO in hPSC-CMs, we first assessed the transport proteins that shuttle LCFAs across the plasma and mitochondrial membranes and the enzymes that catalyze LCFA β-oxidation. CD36 is the primary LCFA transporter on the plasma membrane and is responsible for 70% of LCFA entry into the cell (Coburn et al., 2000; Glatz et al., 2016). Furthermore, CD36 was recently identified as a marker for more mature hPSC-CMs (Funakoshi et al., 2021; Poon et al., 2020). Control hPSC-CMs expressed low levels of cell-surface CD36, suggesting that LCFA uptake may be limited with current differentiation strategies (Figures 4A and 4B). Consistent with the increased *CD36* gene expression, PPARd induction increased CD36 expression by 13.36-fold. In addition to serving as a substrate for FAO, LCFAs can act as PPAR ligands, and LCFA supplementation has been previously shown to enhance hPSC-CM maturation (Yang et al., 2019). We observed a moderate increase in CD36 expression in LCFA-supplemented cultures; however, this increase is lower than what can be achieved via PPARd activation, and it is not dependent on LCFA concentration (Figures 4B and S4A). We confirmed the reproducibility of CD36 regulation in two additional hPSC lines (hiPSCs and hESCs) (Figures S4B and S4C). We next generated atrial hPSC-CMs to investigate the effect of PPARd activation in nonventricular cell types (Devalla et al., 2015; Lee et al., 2017a; Zhang et al., 2011). We demonstrated that CD36 is also low in atrial hPSC-CMs, and that PPARd activation induces CD36 to similar extents as in ventricular hPSC-CMs, suggesting that this is a mechanism common to different CMs (Figure 4C). After crossing the cell membrane, LCFAs are activated to acyl-CoA esters, enter the mitochondria via the carnitine shuttle,

and are subsequently processed by a series of FAO enzymes. We found VLCAD, the first rate-limiting enzyme in the mitochondria to show both increased and more widespread expression across the CMs (Figure 4D). Moreover, FAO, particularly for LCFAs with greater than 20 carbons, occurs in both mitochondria and peroxisomes. We assayed peroxisome abundance and localization using IF and flow cytometry quantification of a peroxisomal protein, PMP70, and detected significantly increased peroxisome content after PPARd activation (Figures S4D and S4E).

In conclusion, we show that PPARd activates the FAO machinery in hPSC-CMs by increasing LCFA transporters and key FAO enzymes, as well as the total peroxisome content, thus facilitating both the uptake and utilization of LCFAs in both atrial and ventricular hPSC-CMs.

PPARd activation enhances OXPHOS in hPSC-CMs

Increased mitochondrial content is a hallmark of CM maturation, as mature CMs require more mitochondria in close proximity to the contractile apparatus to rapidly provide the energy required for contraction. Accordingly, PPARd induction leads to increased mitochondrial content and a greater distribution of mitochondria from the perinuclear localization observed in control hPSC-CMs to a more widespread distribution across the cell and specifically in between sarcomere structures (Figures 5A–5C). We assessed the mitochondrial structure using transmission electron microscopy (TEM) analysis and morphometric quantification of TEM images. Both PPARd activation and LCFA supplementation increased mitochondrial surface area, with the greatest change observed in PPARd activation in the presence of LCFAs (Figures 5D and 5E). Similarly, only LCFA in combination with PPARd activation significantly increased both mitochondrial length and width (Figures 5F and S5A). Mitochondrial cristae organization was enhanced in PPARd-induced hPSC-CMs, which is indicative of highly active and more mature mitochondria (Figure S5B). Lastly, we found *MFN2*, a key driver of mitochondrial fusion, to be upregulated in PPARd-activated hPSC-CMs, while *DNM1*, a regulator of mitochondrial fission, remained unchanged (Figure S5C).

To determine metabolic capacity, we quantified oxygen consumption rates (OCRs) and LCFA oxidation. Basal respiratory capacity was similar in all conditions (Figure S5D). However, PPARd-activated hPSC-CMs had increased maximal respiration and mitochondrial spare capacity, indicative of an augmented capacity to generate ATP upon increased metabolic demand (Figures 5G, 5H, and S5D). Increased maximal respiration and spare capacity were also observed in hPSC-CMs treated with LCFAs and GSK0660. OXPHOS measured in the Seahorse Mito stress test is an incomplete metric of active FAO, as it measures both glucose- and LCFA-derived oxidation. We thus measured the extent of FAO more specifically by quantifying the rate of radiolabeled [9,10-^{3}H]-palmitate oxidation (Doulias et al., 2013). In correlation with our previous findings, PPARd activation led to a significant increase in FAO flux compared with control hPSC-CMs (Figure 5I).

Collectively our data demonstrate that PPARd activation promotes FAO by improving the ability of hPSC-CMs to uptake and metabolize LCFAs, while simultaneously limiting the

contribution of glucose-dependent ATP production, thus inducing the metabolic switch that is characteristic of metabolic maturation during heart development.

PPARd signaling activation enhances electrophysiological and contractile maturation in hPSC-CMs

Over the course of heart development, myocardial compaction, and the systemic pressure of blood flow enhance contractility of the heart, coinciding with increases in PPAR signaling activity at midgestation (Uosaki et al., 2015). To assess cardiac electrophysiology and contractility after PPARd manipulation, we performed action potential (AP) and Ca^{2+} transient (CaT) analysis in single cells and contractility measurements in engineered heart tissues (EHTs). hPSC-CMs were dissociated and plated 4 weeks after PPARd activation or inhibition and paced at 0.5 Hz for all measurements. PPARd activation resulted in increased AP durations, with and without LCFA supplementation (Figures 6A, 6B, and S6A). CaT analysis also demonstrated significant differences in the 20^{th} and 50^{th} percentiles of the intracellular calcium transient duration and decreased decay time and an overall reduction in CaD90, indicative of rapid and efficient release of calcium for contraction (Figures 6C, 6D, and S6B). Previous *in vitro* maturation protocols have resulted in similar changes to the AP and in CaT (Correia et al., 2017, 2018; Tiburcy et al., 2017). To study PPARd-dependent effects on cardiac function in connected cells we performed multielectrode array (MEA) analysis on FACS-isolated hPSC-CMs and found no changes in conduction velocity after PPARd activation or inhibition (Figure S6C). In summary, our comprehensive electrophysiology analysis suggests that PPARd activation improves aspects of electrophysiological maturation in hPSC-CMs.

Finally, we explored the effect of PPARd modulation in 3D EHTs, which represent a physiologically relevant model system for measuring *in vitro* cardiac contractility (Mannhardt et al., 2017; Ruan et al., 2016; Schaaf et al., 2014). EHTs were generated at day 20 of differentiation, allowed to compact for 2 weeks after which PPARd was induced/inhibited for 4 weeks (Figure 6E). EHTs in all conditions showed the anticipated increase in developed force over the 4 weeks, with an average 1.48-fold increase across all EHTs, and no difference in tissue compaction or gross EHT morphology (Figure 6F; Video S1). Neither PPARd activation nor inhibition affected the spontaneous developed force in EHTs between weeks 1 and 4 of treatment (Figure 6G). At a paced beat frequency of 1.0 Hz, the developed force, the ratio of time to the 90^{th} percentile of relaxation (T2Rlx90) relative to the time to peak (T2Pk), and the maximum capture frequency across EHTs remained unchanged across treatment conditions (Figure 6H). However, both systolic and diastolic forces were significantly increased 4 weeks after PPARd induction and LCFA supplementation (Figure 6H). These data support the changes observed in the AP and CaT measurements and indicate that PPARd activation results in enhanced contractility in hPSC-CMs albeit to amounts that do not reflect adult cardiac tissue forces.

Transient lactate exposure induces permanent effects in hPSC-CMs

Prior to switching to FAO postnatally, the developing heart primarily metabolizes glucose and lactate (Burd et al., 1975; Lopaschuk and Jaswal, 2010; Neely and Morgan, 1974; Piquereau and Ventura-Clapier, 2018; Werner and Sicard, 1987). *In vitro*, the ability of

hPSC-CMs to metabolize lactate has led to widely adopted hPSC-CM enrichment protocols (Tohyama et al., 2013). The effects of inducing lactate metabolism, however, have not been investigated in depth. We compared the transcriptomes of control and lactate-treated hPSC-CMs, and surprisingly, transient lactate treatment resulted in extensive long-term transcriptional effects in hPSC-CMs 4 weeks after the last exposure to lactate. KEGG pathway analyses revealed downregulation of processes such as OXPHOS and galactose metabolism (Figures 7A and 7B). The pentose-phosphate pathway was also downregulated upon lactate exposure, reminiscent of previous work showing that its inhibition results in cardiac maturation (Nakano et al., 2017). Among the changes in metabolism genes, we identified several candidates involved in reducing lactate sensitivity and processing ability (Figure 7C): for example, MCT4 (*SLC16A3*), which transports lactate across the plasma membrane; the glucose transporter GLUT1 (*SLC2A1*); and *LDHA*, *PDHA1*, *HK1*, and *HK2*, which encode additional components involved in lactate turnover and glucose metabolism. Collectively, the downregulation of these genes suggests that a transient pulse of lactate is sufficient to induce long-term changes, including a decreased sensitivity to the substrate. Similar to PPARd induction, transient lactate exposure leads to increased expression of Wnt inhibitors, such as *SFRP1* and *SRFP2*, and a decrease in *Wnt11*, as well as a decrease in proliferation markers *CCND2* and *IGF2*. This is in line with other studies showing that Wnt inhibition and decrease in proliferation are critical for cardiac maturation (Buikema et al., 2020). Lastly, we observed increased expression of genes underlying cardiac contractility (*TNNT2*, *MYLK,* and *MYOM3*) and calcium signaling (*CACNA1C* and *CASQ2*) (Figure 7C). These analyses suggest that the transient lactate exposure commonly used in the lactate selection protocol result in lasting changes to hPSC-CMs, potentially driving contractile maturation without enhancing metabolic maturation.

PPARd induction induces a metabolic switch across multiple cell-culture formats

We next tested whether PPARd is able to effectively induce the metabolic switch in multiple culture formats frequently used by the field. We induced and inhibited PPARd signaling in lactate-purified hPSC-CMs and EHTs for 4 weeks and performed RNA-seq of FACS-isolated CMs (SIRPA+CD90−). PPARd induction in both lactate-exposed and EHT hPSC-CMs resulted in the metabolism-focused transcriptional response previously observed in 2D monolayer cells, including increased expression of LCFA transporters (*CD36* and *CPT1A*), key FAO enzymes (*ACADVL*, *ANGPTL4*, *HADHA*, *HADHB*, *ACSL1*, and *PDK4*), and the FA metabolism, OXPHOS, and peroxisome KEGG pathways (Figures 7C, 7D, and S7). Interestingly, both baseline expression (control and untreated) and the extent of differential gene expression after PPARd induction varied between culture formats, suggesting that each format results in differential baseline metabolic activities and varying abilities to induce a metabolic switch upon PPARd induction. This confirms studies demonstrating that tissue formats can induce both contractile and metabolic maturation in the absence of any additional modifications (Ronaldson-Bouchard et al., 2018; Ulmer and Eschenhagen, 2020). In summary, transcriptional profiling across hPSC-CM culture formats confirms that PPARd activation reliably induces a metabolic switch, thus providing an approach to enhance metabolic maturation broadly and to develop multiparameter strategies for metabolic and contractile maturation *in vitro*.

DISCUSSION

In this study, we leveraged key mechanisms for heart development *in vivo* that are not recapitulated in current differentiation protocols to enhance hPSC-CM maturation. Despite the important advances that have been made by many groups (Table S3), the field lacks easy and broadly applicable strategies that result in stable, long-term maturation.

We hypothesized that the incomplete recapitulation of early signaling environments during heart development was limiting hPSC-CM maturation and focused on the PPAR signaling pathway, which is known to regulate metabolism, proliferation, and the immune response (Lee and Kim, 2015; Lopaschuk and Jaswal, 2010). While previous work in hPSCs has primarily focused on the most prominent isoform in the heart, PPARa, the distinct gene expression patterns and mouse KO phenotypes indicate that isoform specificity exists (Funakoshi et al., 2021; Gentillon et al., 2019; Murphy et al., 2021; Poon et al., 2015; Uosaki et al., 2015). By assaying each PPAR isoform separately, we found that PPARa is most abundantly and highly expressed and is critical for hPSC-CM differentiation and maintenance, suggesting that it is both active and required in current differentiation protocols. However, additional PPARa activation using PPARa agonists did not enhance cardiac maturation, perhaps because PPARa is already at its most efficient level. Other studies that activated PPARa have done so in combination with additional modifications (e.g., LCFAs and T3), or used agonists at a range of concentrations up to 20-fold higher than those used here (Funakoshi et al., 2021; Gentillon et al., 2019; Poon et al., 2015). PPARg did not impact *in vitro* maturation, in line with its predominant role in adipose tissue and its low expression in the heart (Braissant and Wahli, 1998; Kliewer et al., 1994; Lee and Kim, 2015). Of the three isoforms, PPARd activation resulted in the most prominent induction of maturation, as described in more detail below.

Supplying LCFAs alone has been shown to induce hPSC-CM maturation (Batho et al., 2020; Mills et al., 2017; Slaats et al., 2020; Yang et al., 2019). Our data suggest that the effects of substrate alone are indeed present and that combining LCFAs with PPARd activation leads to a stronger activation of the FAO machinery and, consequently, a more efficient activation of the metabolic switch. LCFAs alone may not have a larger effect due to CPT1 activity, which is an indicator of when organisms begin to use LCFAs (Ascuitto and Ross-Ascuitto, 1996; Fisher, 1984; Warshaw and Terry, 1970). For example, isolated newborn pig hearts obtain 90% of their energy from the metabolism of circulating FAs, and LCFA perfusion increases tissue levels of acyl-carnitines (Fisher, 1984; Werner et al., 1983). In many other mammals, however, CPT1 enzymatic maturation does not occur until after birth (Barrie and Harris, 1977; Tomec and Hoppel, 1975; Warshaw and Terry, 1970; Wittels and Bressler, 1965). PPARd activation with LCFA supplementation increases *CPT1B* expression, the muscle-specific CPT1 isoform, but there are no significant increases with either LCFAs or PPARd alone. In the absence of increased CPT1B activity, LCFAs alone are thus unlikely to positively contribute to hPSC-CM FAO.

Improved cardiac contractility is an important hallmark of cardiac maturation and is supported by structural, metabolic, and electrophysiological changes. Our electrophysiological measurements demonstrated quantitatively that PPARd induction

resulted in an overall shortened CaT but an increase in duration of the peak of the Ca waveform. This likely contributed to the increase in the plateau phase of the AP and indicates efficient release of calcium for contraction. This study would benefit from further electrophysiological characterization using patch-clamp analysis to quantify resting membrane potential and upstroke velocity, which cannot be measured using fluorescence-based AP/CaT assays. Previous studies have shown that EHTs enhance maturation, including increased contractility and metabolic activity (Lemoine et al., 2017; Ronaldson-Bouchard et al., 2018; Tiburcy et al., 2011; Turnbull et al., 2014; Ulmer and Eschenhagen, 2020; Ulmer et al., 2018). We hypothesized that PPARd-mediated maturation would increase available energy levels and thus improve cardiac contractility in EHTs. We observed increases in systolic and diastolic force following PPARd induction, the former of which is likely driven by sustained release of calcium at the plateau phase, but these changes are smaller than those reported in similar studies. This may be due to the later time points we used when EHTs had likely matured in culture over time (Kosmidis et al., 2015; Nakano et al., 2017; Parikh et al., 2017; Yang et al., 2014b). Future studies should investigate the magnitude of PPARd-mediated maturation in comparatively younger cells and tissues. Furthermore, assaying contractility in 3D models can be impacted by cellular heterogeneity, varying stiffnesses, and extracellular matrix properties (Lee et al., 2017b), and contractility measurements on patterned single cells may represent a reliable alternative (Paige et al., 2020).

Glucose deprivation has been linked to enhanced cardiac maturation and is part of the widely adopted lactate selection protocol (Nakano et al., 2017; Tohyama et al., 2013). Our data demonstrate enhanced FAO in the presence of glucose. We thus investigated the effect of transient lactate exposure to explore the additive effects of glucose deprivation with PPARd activation on hPSC-CM maturation. We observed an unexpected reduction in the expression of components of the lactate transport and oxidation machinery, suggesting that hPSC-CMs display a reduced ability to uptake and process lactate as a metabolic substrate. Similar effects were described in isolated human skeletal muscle cells (Lund et al., 2018). Lactate exposure further led to downregulation of genes involved in glycolysis and the pentose-phosphate pathway and resulted in a long-term reduction of *LDH-A* expression—outcomes that have previously been linked to maturation of hPSC-CMs (Hu et al., 2018; Nakano et al., 2017). We also found that activating PPARd in lactate-treated hPSC-CMs induces FAO in lactate-selected hPSC-CMs, while maintaining the gene expression changes induced upon lactate exposure alone. This illustrates the breadth of metabolic regulation within the human heart where different metabolic perturbations can have distinct and additive effects during hPSC-CM maturation.

In conclusion, we show that PPARd activation recapitulates key developmental stages of heart development in hPSC-CMs by activating the metabolic switch from glycolysis to FAO (Table S3). PPARd activation in fully differentiated hPSC-CMs leads to stable long-term changes and therefore represents an *in vitro* maturation protocol that is easily implemented and broadly applicable across many cardiac differentiation strategies. Reliable *in vitro* maturation of hPSC-CMs addresses a major current roadblock and will expand the opportunities for relevant drug discovery, toxicology studies, and human disease modeling.

Limitations of the study

We used hPSC-CMs that were approximately 10 weeks old at the time of analysis. As such, evaluating cardiac maturation in our protocol relative to published literature that typically used earlier time points is challenging, especially given the considerable changes in maturation parameters that are related to prolonged culture (Table S2; Feyen et al., 2020; Funakoshi et al., 2021; Hu et al., 2018; Nakano et al., 2017; Poon et al., 2020; Tiburcy et al., 2017). This may explain, for example, the modest effect of LCFA alone, yet strengthens the extensive and stable changes induced by PPARd activation (Correia et al., 2017; Feyen et al., 2020; Funakoshi et al., 2021; Hu et al., 2018; Murphy et al., 2021; Parikh et al., 2017; Yang et al., 2019). A technical limitation of the study is the lack of patch-clamp analysis, which would provide a complete evaluation of PPARd-mediated changes in electrophysiology. Lastly, translational studies into disease modeling or drug discovery would be required to understand the full potential of PPARd activation for *in vitro* hPSC-CM maturation.

STAR★METHODS

RESOURCE AVAILABILITY

Lead contact—Further information and requests for resources and reagents should be directed to and will be fulfilled by the lead contact, Dr. Nicole Dubois (nicole.dubois@mssm.edu).

Materials availability—This study did not generate new unique reagents.

Data and code availability

- RNAseq and ATACseq data have been deposited at GEO and are publicly available as of the date of publication. Accession numbers are listed in the key resources table. RNAseq data can be searched in the publicly accessible RNASeq Resource Website (link listed in key resources table).
- This paper does not report original code.
- Any additional information required to reanalyze the data reported in this paper is available from the lead contact upon request.

EXPERIMENTAL MODEL AND SUBJECT DETAILS

Human pluripotent stem cell lines—The following hPSC lines were used in the study: MSN02-4 (induced pluripotent stem cell line, female, generated from skin biopsy harvested at 36 years of age, generated at the Icahn School of Medicine at Mount Sinai), H9 (WA09, human embryonic stem cell line, female, derived from blastocyst stage), and WTC11 (induced pluripotent stem cell line, male, generated from skin biopsy harvested at 30 years of age, purchased from Coriell Institute) (Schaniel et al., 2021). hPSCs were maintained in E8 medium with daily feeding and passaged every 4 days onto matrigel-coated plates (Roche). They were dissociated to single cells using EDTA (Corning) and replated at a 1:6 ratio. All of the work with human PSCs was approved by the Embryonic Stem Cell Research Oversight Committee (ESCRO) at Mount Sinai.

Human developing heart tissues—De-identified, non-anomalous second trimester human fetal heart tissue was obtained from elective terminations through the ISMMS Biorepository and Pathology Core (HS#12-00145) at the Icahn School of Medicine at Mount Sinai. All of the work using fetal tissue was approved by the Bioethics Program at the Icahn School of Medicine at Mount Sinai.

METHOD DETAILS

Human pluripotent stem cell differentiation—On Day 0 (start of differentiation) hPSCs were incubated with 1 mg/ml Collagenase B (Roche) for one hour, or until cells dissociated from plates, to generate embryoid bodies (EBs). Cells were collected and centrifuged at 300 rcf for 3 min, and resuspended as small clusters of 50–100 cells in differentiation medium consisting of RPMI (Gibco), 2 mmol/L L-glutamine (Invitrogen), 4×10^4 monothioglycerol (MTG, Sigma-Aldrich) and 50 μg/ml ascorbic acid (Sigma-Aldrich). Differentiation medium was supplemented with 2 ng/ml BMP4 and 3 μmol Thiazovivin (Milipore). EBs were cultured in 6 cm dishes (USA Scientific) at 37°C in 5% CO^2, 5% O^2, and 90% N^2. On Day 1, the medium was changed to differentiation medium supplemented with 30 ng/ml BMP4 (R&D Systems) and 30 ng/ml Activin A (R&D Systems), 5 ng/ml bFGF (R&D Systems) and 1 μmol Thiazovivin (Milipore). On Day 3, EBs were harvested and washed once with DMEM (Gibco). Medium was changed to differentiation medium supplemented with 5 ng/ml VEGF (R&D Systems) and 5 μmol/L XAV (Stemgent). On Day 5, medium was changed to differentiation medium supplemented with 5 ng/ml VEGF (R&D Systems). After Day 8, medium was changed every 3–4 days to differentiation medium without supplements.

Cell dissociation, plating, and treatments—EBs were dissociated on day 20 of differentiation. EBs were incubated overnight with 0.6 mg/ml Collagenase Type II (Worthington) at 37°C (Dubois et al., 2011). Dissociated cells were harvested and washed with Wash medium (DMEM, 0.1% BSA) + 1mg/ml DNase (VWR) twice and centrifuged at 300 rcf for 3 mins. Cells were resuspended in differentiation medium supplemented with 1 μmol Thiazovivin (Millipore), filtered and counted using a hemacytometer. hPSC-CMs were plated onto matrigel-coated plates at appropriate cell densities (6 well plate – 1,000,000 cells/well; 12 well plate – 700,000 cells/well; 48 well plate – 150,000/well; 96 well plate – 80,000 cells/well; 22×22mm coverslips for immunofluorescence – 35,000 cells/cover slip; 22×22mm coverslips for Calcium transients – 25,000 cells/cover slip). Medium was removed the following day and replaced with differentiation medium. Medium was changed every 2 days. Two weeks after plating differentiation medium was supplemented with small molecules (GSK0660 (Sigma-Aldrich, 2.5 μM), GW0742 (Sigma-Aldrich, 5 μM), Rosiglitazone (Sigma-Aldrich, 5 μM), WY14643 (Sigma-Aldrich, 5 μM) with or without BSA-complexed long-chain fatty acids (LCFAs: FA-free BSA (Sigma-Aldrich), Palmitic Acid (Sigma-Aldrich, 12.5 mM), Oleic Acid (Sigma-Aldrich, 12.5 μM), Linoleic Acid (Sigma-Aldrich, 12.5 μM); LCFAs used in 5:4:1 ratio) for 4 weeks.

Lactate treatment—EBs were dissociated as described above and plated on Matrigel-coated 12 well plates at 700,000 cells/well in differentiation medium supplemented with 1 μmol Thiazovivin (Millipore). Medium was removed the following day and replaced

with differentiation medium. After 3 days, differentiation medium was replaced with lactate medium (Stock Solution: 1 M lactate, 1 M Na-Hepes in distilled water; Working solution: 4mM lactate in DMEM -Glucose) for 4 days (Tohyama et al., 2013). From days 5–8, lactate medium was titrated down in the following lactate-medium: differentiation-medium ratios: Day 5: 3:1; Day 6: 1:1; Day 7: 1:3; Day 8: 0:4.

Engineered heart tissue protocols—EBs were dissociated by incubation with 0.6 ml/ml Collagenase Type II (Worthington) for two hours at 37°C and washed with Wash medium (DMEM, 0.1% BSA) + 1mg/ml DNase (VWR) twice and centrifuged at 300 rcf for three 3 mins. Cells were resuspended in TrypLE Express (Gibco), incubated at 37°C for three mins, washed with Wash medium (DMEM, 0.1% BSA) + 5mg/ml DNase (VWR) and centrifuged at 300 rcf for three mins. Cells were resuspended in differentiation medium supplemented with one μmol Thiazovivin (Millipore), filtered and counted using a hemacytometer. Engineered Heart Tissues (EHTs) were generated as previously described (Schaaf et al., 2014). Briefly, a cell-suspension of 1,000,000 cells, 2.5 μl Fibrinogen (Sigma-Aldrich), 3 μl Thrombin (Biopur) in 100μl differentiation medium per EHT were pipetted into molds made of 2% agarose. EHTs were then maintained in differentiation medium + Aprotinin (Sigma-Aldrich). To dissociate, EHTs were removed from posts with tweezers and dissociated overnight at 37°C in 0.6 mg/ml Collagenase Type II (Worthington). Dissociated cells were harvested and washed with Wash medium (DMEM, 0.1% BSA) + 1 mg/ml DNase (VWR) twice and centrifuged at 300 rcf for three mins. Cells were resuspended in differentiation medium supplemented with one μmol Thiazovivin, filtered and counted using a hemacytometer.

Immunofluorescence analysis

Tissue embedding and cryosectioning: Fetal heart tissue was fixed in 4% paraformaldehyde overnight, washed with PBS, equilibrated in 30% sucrose (Sigma-Aldrich) and embedded in OCT (Electron Microscopy Services). Tissues were cut at 5 μM using a Leica Cryostat.

Immunofluorescence analysis: Cells plated on 22×22mm coverslips or tissue cryosections were rinsed with PBS and fixed with 4% paraformaldehyde for 10 mins at room temperature. The edges of the coverslips were marked with a hydrophobic pen. Fixed cells were blocked with Saponin buffer (PBS, 0.5% Saponin, 0.1% BSA) for one hour at room temperature, incubated in primary antibody solution in Saponin buffer overnight at 4°C or for one hour at room temperature. Cells were rinsed three times with Saponin buffer, resuspended in secondary antibody diluted in Saponin buffer and incubated for one hour at room temperature. Cells were rinsed three times with Saponin buffer. Coverslips were mounted onto slides with nPG Antifade mounting medium (nPG stock : Glycerol : 10X PBS in the ratio 1:90:10) and edges were sealed with nail polish (VWR).

Primary antibody dilutions: Anti-α-Actinin (Sigma-Aldrich, 1:100), Anti-Cardiac Troponin T (Abcam, 1:400), Anti-PPARa (Santa Cruz, 1:100), Anti-PPARd (Thermo Fisher, 1:100), Anti-PPARg (Santa Cruz, 1:100), Anti-ACADVL (Abcam, 1:50), MitoTracker Deep Red dye (Thermo Fisher, 1:10,000), Anti-PMP70 AF488 (Fisher Scientific, 1:500).

Secondary antibody dilutions: Alexa Fluor dyes (Jackson Immunoresearch) were diluted in Saponin buffer at 1:500.

Image acquisition and processing: All images were acquired on a Leica DM5500 inverted microscope and processed for brightness and contrast using Fiji (Schindelin et al., 2012).

Image analysis: cTNT images were quantified using the MatLab-based software, MatFiber (Fomovsky and Holmes, 2010). MatFiber analyzes intensity gradients in immunofluorescent images to determine alignment (Mean Vector Length, MVL) and the circularity standard deviation (CSD). Custom FIJI and R scripts were used to determine the distance between alpha actinin+ Z-disks.

Flow cytometry analysis and fluorescence-activated cell sorting (FACS)

Live flow cytometry and FACS: Dissociated cells were resuspended for 30mins on ice in differentiation medium containing antibodies (dilutions listed below). Cells were washed with differentiation medium and resuspended in differentiation medium + DAPI (1.35μg/ml, Biolegend) for flow cytometry analysis (BD LSRIIA, BD FACSCelesta) or FACS (BD FACSAria).

Fixed flow cytometry: Dissociated cells were fixed with 4% paraformaldehyde for 10 mins at room temperature. Fixed cells were blocked in Saponin buffer (PBS, 0.5% Saponin, 0.1% BSA) for one hour at room temperature and resuspended in primary antibody solution in Saponin buffer overnight at 4°C. Cells were rinsed with Saponin buffer, resuspended in secondary antibody solution in Saponin buffer and incubated for one hour at room temperature. Cells were rinsed with saponin buffer and resuspended in flow buffer + DAPI for flow cytometry.

Antibody dilutions: PE-Cy7 anti-human CD172a/b (SIRPalpha/beta, Biolegend, 1:200), PE anti-human CD90 (Biolegend, 1:200), APC anti-human CD36 (Biolegend, 1:100), Mito Tracker Deep Red dye (Thermo Fisher, 1:10,000; binds mitochondria in a delta-psi independent manner), Anti-Cardiac Troponin T (Abcam, 1:400), PMP70 AF488 (Fisher Scientific, 1:500).

cDNA generation and real-time qPCR—RNA was isolated from cells/tissues using the Quick-RNA kit (Zymo Research). cDNA was generated using reverse transcription with the Quanta qScript kit (Quanta bio). Quantitative PCR was carried out on an Applied Biosystems Step One Plus using ABI SYBR Green reagents. Expression levels were normalized to TATA-binding protein (TBP) and genomic DNA was used for quantification of absolute expression levels, as previously described (Dubois et al., 2011).

Bulk RNA-sequencing—RNA was extracted from FACS-isolated SIRPA+CD90- hPSC-CMs using the Quick RNA Micro kit (Zymo Research) for all samples analyzed in this study. 500 ng of RNA per sample was used for Automated RiboZero Gold library prep and sequenced using a S2 100 cycle flow cell. FASTQ files were aligned with kallisto to a reference transcriptome model generated from the human genome hg38 using default parameters (Bray et al., 2016). The average number of reads successfully pseudoaligned

across samples was 16.46 million, with a standard deviation of 3.76 million. DESeq2 was used to normalize read counts and determine differentially expressed genes with $p<0.05$. GAGE was used to identify GO and KEGG pathways that were upregulated or downregulated with $p<0.05$. Custom R scripts were used to generate heatmaps. Published code was adapted to generate UpsetR plots, KEGG comparisons and Chord Plots (Lex et al., 2014).

Single cell RNA-sequencing—Lactate-treated hPSC-CMs were plated in 48 well Matrigel-coated plates at a density of 250,000 cells/well. After 2 weeks in culture cells were dissociated by incubation with 0.6 ml/ml Collagenase Type II (Worthington) for two hours at 37°C, washed with Wash medium (DMEM, 0.1% BSA) + 1mg/ml DNase (VWR) twice and centrifuged at 300 rcf for three 3 mins. Cells were resuspended in differentiation media and counted using a hemacytometer. Libraries were generated using the Chromium platform with the 3' gene expression (3' GEX) V3 kit, using an input of ~10,000 cells. Gel-Bead in Emulsions (GEMs) were generated on the sample chip in the Chromium controller. Barcoded cDNA was extracted from the GEMs by Post-GEM RT-cleanup and amplified for 12 cycles. Amplified cDNA was then fragmented and subjected to end-repair, poly A-tailing, adapter ligation, and 10X-specific sample indexing following the manufacturer's protocol. Libraries were quantified using Bioanalyzer and QuBit analysis. Libraries were sequenced in paired end mode on a NovaSeq instrument targeting a depth of 50,000 reads per cell. Sequencing data was aligned and quantified using the Cell Ranger Single-Cell Software Suite (version 3.0, 10x Genomics) against the provided hg38 human reference genome. Downstream differential expression and clustering analysis was performed using the Seurat V.4.0 package, as described in the tutorials (http://satijalab.org/seruat/). *cellRanger* matrices were imported for each sample, and distributions of nCountRNA, nFeatures and % mitochondrial gene expression were examined for each sample in order to filter out doublets or cells of low quality. Cells with greater than 20% of genes coming from mitochondrial genes were selected against, as well as those with fewer than 200 genes. The resulting subset Seurat objects were normalized using the scTransform workflow and further scaled and normalized the RNA assay in order to perform downstream differential expression analysis and marker visualization utilizing the FindMarkers and FeaturePlot functions on the RNA assay. We performed principal component analysis using the highly variable genes for each sample. The most significant principal components (20–30 depending on sample) were used for graph-based unsupervised clustering (FindClusters and FindNeighbor functions). Uniform manifold approximation and projection (UMAP) was performed using a standard resolution parameter of 0.5 and iteratively modified after performing marker gene expression and examining expression of key markers.

ATAC sequencing—ATAC-seq was performed as described in (Buenrostro et al., 2015). Briefly, cells were FACS-isolated and split into aliquots of 50,000 cells from each sample. After washing with PBS, samples were resuspended in cold lysis buffer (10 mM Tris-HCl pH 7, 10 mM NaCl, 3 mM $MgCl_2$, 0.01% Igepal CA-630) and spun down at 500 x g for 10 min at 4°C. Cells were incubated with 25 μL TD buffer, 2.5 μL Tn5 transposase (Illumina; Cat No: #20034198) and 22.5 μL nuclease-free H_20 at 37°C for 30 min with gentle agitation. After purification (Qiagen; Cat No: #28004), transposed DNA fragments were

amplified with custom PCR primers (Buenrostro et al., 2013) for a total of 9 cycles. The final PCR cycle number needed to minimally amplify libraries was determined by a separate qPCR reaction as described in Buenrostro et al. (2015) to minimize GC and size bias. Purified libraries were sequenced on an Illumina Novaseq 6000. Adapters were trimmed from the raw fastq data with cutadapt, and the raw data was aligned to hg38 with bwa mem. PCR duplicates were removed with Picard, in addition to reads mapping to mitochondrial sequences or known problematic genomic regions in the ENCODE blacklist. Macs2 was used to call peaks with the bampe parameter. To reduce false positives, peaks were used when overlapping with consensus regions mapped in at least two samples. Featurecounts was used to count reads associated with known promoter regions or candidate regulatory elements listed in the SCREEN (Search Candidate cis-Regulatory Elements by ENCODE) database. DESeq2 was used to identify differential peaks with $p<0.05$, and peaks were annotated with the closest genes.

Seahorse analysis—Dissociated cells were plated at 25,000 cells per well in a 96-well microplate (Agilent). One week after plating, an XF Cell Mito Stress Test (Agilent, Oligomycin 1 μM, FCCP 2 μM, Rotenone and Antimycin A 0.5 μM) was performed using an XFe96 Analyzer. Cell numbers were normalized using Methylene Blue staining and normalized data were analyzed using Seahorse Wave Desktop Software.

Fatty acid oxidation flux assay—The FAO flux assay quantifies the rate of [9,10-^{3}H] Palmitate (PerkinElmer, Waltham, MA) oxidation. [9,10-^{3}H] Palmitate was emulsified in Kreb/BSA solution (4.5 mg/ml) to a final concentration of 23 μM (Master Mix) overnight at 37° C under continuous agitation. FACS-isolated SIRPA+CD90- hPSC-CMs were seeded in a 96-well plate (80,000cell/well) and were incubated for 4h with 200 μl Master Mix. The ^{3}H2O released into the cell medium was quantified. Etomoxir (2[6(4-chlorophenoxy) hexyl]oxirane-2-carboxylate, 10 μM) an irreversible inhibitor of carnitine palmitoyltransferase-1 (CPT-1a) was used to document the mitochondrial-dependent β-oxidation of palmitate. The flux is expressed in pmol/h/mg protein.

Multi-electrode array analysis—Dissociated and FACS-isolated SIRPA+CD90- hPSC-CMs were plated at 60,000 cells per well in a CytoView 48-well multielectrode array (MEA) plate (Axion Biosystems). One week after plating recordings were taken using an Axion Integrated Studio (AxIS) on the Axion Maestro. Cardiac Beat Detector measurement parameters were set at 300 μV detection threshold, 250 ms min. beat period, 5s max. beat period, polynomial regression FPD detection method, 70 ms post-spike detection holdoff, 50 ms pre-spike detection holdoff, 1s match post search duration with limit FPD search, and 10 running average beat count used for FPD detection.

Electrophysiology measurements—FACS-isolated SIRPA+CD90- hPSC-CMs were plated at 30,000 cells/coverslip (Sarstedt). 7 days post-plating AP and CaT measurements were performed using voltage and Ca2+ sensitive dyes. Briefly, coverslips were incubated in 1X Tyrodes' buffer (140 mM NaCl, 5.4 mM KCl, 10mM HEPES, 1 mM NaH2PO4, 1 mM MgCl2, 10 mM Glucose and 1.8 mM CaCl2, calibrated to pH=7.4) containing 10 mM Calbryte-630 AM (AAT Bioquest) and Fluovolt dyes (Invitrogen – dilution 1:1000

Fluovolt dye, 1:100 Powerload concentrate) in order to get paired AP and CaT recordings from a single coverslip. Coverslips were incubated in dye solution for 30 minutes at 37°C. Coverslips were then transferred to custom cassette insert and incubated in 1X Tyrode's buffer with 10 mM blebbistatin for 5 minutes, then loaded onto microscope for measurement. Tyrodes' buffer was perfused throughout measurement to maintain cells at 37°C. Cells were paced at 0.5 Hz using a MyoPacer Field Stimulator. 10–15 cells were recorded per coverslip across three biological replicates, resulting in a total of 30–45 cells per condition. Recordings of fluorescence flux in line scan were taken on an LSM5 exciter microscope using Zeiss ZEN 2009 software. Image files were analyzed using custom MATLAB scripts to extract features from individual waveforms for quantification.

Engineered heart tissue deflection analysis—Engineered Heart Tissues (EHTs) were generated using established protocols and described above (Schaaf et al., 2014). 14 days post-fabrication, contractile function was measured every week for 5 weeks (from Week 0–4 of treatment). At the day of measurement, pacing electrodes were positioned along each array of tissues and the plate was put into the incubator to equilibrate (Mannhardt et al., 2017). After 30 minutes, the plate was placed on a stage equipped with a right angle mirror reflecting the image of the EHT posts to a dissecting microscope and high-speed camera (Turnbull et al., 2018). LabVIEW software was used to acquire real-time data of post deflection, by applying a beam-bending equation from elasticity theory as previously described (Serrao et al., 2012). The data were analyzed with a custom MATLAB script to calculate twitch parameters including developed force (DF; calculated from the post deflection with each twitch), maximum contraction rate (+dF/dt) and maximum relaxation rate (-dF/dt), as previously described (Turnbull et al., 2014). Functional data were first recorded under spontaneous conditions, including measuring spontaneous beating rate. For paced measurements the electrodes were connected to a S88X Grass Stimulator (Astro-Med, Inc., West Warwick, RI) and data were recorded under electrical stimulation, at rates from 0.25 Hz to 3.0 Hz with 0.25 Hz increments. At the end of each day of recording, the electrodes were removed and medium was replaced with fresh medium.

Transmission electron microscopy—Dissociated cells were plated onto 22×22 mm coverslips such that they covered the majority of the coverslip surface. The cells were fixed with 2% paraformaldehyde and 2% glutaraldehyde/PBS, pH 7.2 for a minimum of one week at 4°C. Sections were rinsed in 0.1 M sodium cacodylate buffer (EMS), fixed with 1% osmium tetroxide followed with 2% uranyl acetate, dehydrated through ascending ethanol series (beginning with 25% up to 100%) and infiltrated with Embed 812, an epon resin kit (EMS). Beem capsules (EMS) were placed on top of the cells, filled with resin, and heat polymerized at 60 degrees C for 72 hrs. Post polymerization, capsules were heated to 60°C for 3.5 minutes and snapped from the substrate to dislodge the cells. Semithin sections (0.5 and 1 μm) were obtained using a Leica UC7 ultramicrotome, counterstained with 1% Toluidine Blue, cover slipped and viewed under a light microscope to identify successful dislodging of cells. Ultra-thin sections (80nms) were collected on nickel 300 mesh grids (EMS) using a Coat-Quick adhesive pen (EMS). Sections were counter-stained with 1% uranyl acetate followed with lead citrate, and imaged on an Hitachi 7000 electron microscope (Hitachi High-Technologies, Tokyo, Japan) using an advantage CCD camera

(Advanced Microscopy Techniques, Danvers, MA). Images were adjusted for brightness and contrast using Adobe Photoshop CS4 11.0.1.

QUANTIFICATION AND STATISTICAL ANALYSIS

Data are presented as mean ± standard deviation. Statistical significance between two groups were determined using two-sided unpaired or paired Student's t-tests. One-way ANOVAs were used when testing for relationships between 3 or more groups with appropriate post-hoc testing. The statistical tests performed are included in the figure legends. Statistical tests were performed using GraphPad Prism 6.

Supplementary Material

Refer to Web version on PubMed Central for supplementary material.

ACKNOWLEDGMENTS

We thank the ISMMS Flow Cytometry Core (Christopher Bare and Xuqiang Qiao), Microscopy Core (William Jansen, Allison Sowa, Esperanza Agullo Pascual, and Shilpa Dilipkumar), Biorepository and Pathology Core (Michael Donovan, Olha Fedorshyn, and Anastasiya Dzuhun), Stem Cell Shared Resource facilities and the NYU Genome Technology Center (Adriana Heguy and Sitharam Ramaswami) for their technical assistance. Drs. Jinqi Gong and Jaehee Shim provided assistance with calcium transient measurements and analysis. Dr. Irene C. Turnbull is ethically opposed to research involving human embryonic stem cells and tissues derived from elective abortions; Dr. Turnbull performed the functional measurements and data analysis of human engineered tissues and instructed on use of MatFiber to quantify myofibril organization. We thank her for her invaluable contributions to this project. This work was funded by NIH/NHLBI R01HL134956 and R56HL128646 and The Mindich Child Health and Development Institute seed funding to N.C.D. N.M.W. was supported by a Training Program in Stem Cell Biology fellowship from the New York State Department of Health (NYSTEM-C32561GG).

REFERENCES

Ahmadian M, Suh JM, Hah N, Liddle C, Atkins AR, Downes M, and Evans RM (2013). PPARγ signaling and metabolism: the good, the bad and the future. Nat. Med. 19, 557–566. [PubMed: 23652116]

Ascuitto RJ, and Ross-Ascuitto NT (1996). Substrate metabolism in the developing heart. Semin. Perinatol. 20, 542–563. [PubMed: 9090780]

Barak Y, Liao D, He W, Ong ES, Nelson MC, Olefsky JM, Boland R, and Evans RM (2002). Effects of peroxisome proliferator-activated receptor δ on placentation, adiposity, and colorectal cancer. Proc. Natl. Acad. Sci. USA 99, 303–308. [PubMed: 11756685]

Barger PM, and Kelly DP (2000). PPAR signaling in the control of cardiac energy metabolism. Trends Cardiovasc. Med. 10, 238–245. [PubMed: 11282301]

Barrie SE, and Harris P (1977). Myocardial enzyme activities in guinea pigs during development. Am. J. Physiol. 233, H707–H710. [PubMed: 596469]

Batho CAP, Mills RJ, and Hudson JE (2020). Metabolic regulation of human pluripotent stem cell-derived cardiomyocyte maturation. Curr. Cardiol. Rep. 22, 73. [PubMed: 32594263]

Bhattacharjee A, Joiner WJ, Wu M, Yang Y, Sigworth FJ, and Kaczmarek LK (2003). Slick (Slo2.1), a rapidly-gating sodium-activated potassium channel inhibited by ATP. J. Neurosci. 23, 11681–11691. [PubMed: 14684870]

Braissant O, and Wahli W (1998). Differential expression of peroxisome proliferator-activated receptor-alpha, -beta, and -gamma during rat embryonic development. Endocrinology 139, 2748–2754. [PubMed: 9607781]

Brandão KO, Tabel VA, Atsma DE, Mummery CL, and Davis RP (2017). Human pluripotent stem cell models of cardiac disease: from mechanisms to therapies. Dis. Model. Mech. 10, 1039–1059. [PubMed: 28883014]

Bray NL, Pimentel H, Melsted P, and Pachter L (2016). Near-optimal probabilistic RNA-seq quantification. Nat. Biotechnol. 34, 525–527. [PubMed: 27043002]

Buenrostro JD, Giresi PG, Zaba LC, Chang HY, and Greenleaf WJ (2013). Transposition of native chromatin for fast and sensitive epigenomic profiling of open chromatin, DNA-binding proteins and nucleosome position. Nat. Methods 10, 1213–1218. [PubMed: 24097267]

Buenrostro JD, Wu B, Chang HY, and Greenleaf WJ (2015). ATAC-seq: a method for assaying chromatin accessibility genome-wide. Curr. Protoc. Mol. Biol. 109, 21.29.1–21.29.9.

Buikema JW, Lee S, Goodyer WR, Maas RG, Chirikian O, Li G, Miao Y, Paige SL, Lee D, Wu H, et al. (2020). Wnt activation and reduced cell-cell contact synergistically induce massive expansion of functional human iPSC-derived cardiomyocytes. Cell Stem Cell 27, 50–63.e5. [PubMed: 32619518]

Burd LI, Jones MDJ, Simmons MA, Makowski EL, Meschia G, and Battaglia FC (1975). Placental production and foetal utilisation of lactate and pyruvate. Nature 254, 710–711. [PubMed: 1124133]

Burridge PW, Holmström A, and Wu JC (2015). Chemically defined culture and cardiomyocyte differentiation of human pluripotent stem cells. Curr. Protoc. Hum. Genet. 87, 21.3.1–21.3.15.

Calderon D, Bardot E, and Dubois N (2016). Probing early heart development to instruct stem cell differentiation strategies. Dev. Dyn. 245, 1130–1144. [PubMed: 27580352]

Cheng L, Ding G, Qin Q, Huang Y, Lewis W, He N, Evans RM, Schneider MD, Brako FA, Xiao Y, et al. (2004). Cardiomyocyte-restricted peroxisome proliferator-activated receptor-[delta] deletion perturbs myocardial fatty acid oxidation and leads to cardiomyopathy. Nat. Med. 10, 1245–1250. [PubMed: 15475963]

Coburn CT, Knapp FF, Febbraio M, Beets AL, Silverstein RL, and Abumrad NA (2000). Defective uptake and utilization of long chain fatty acids in muscle and adipose tissues of CD36 knockout mice. J. Biol. Chem. 275, 32523–32529. [PubMed: 10913136]

Correia C, Koshkin A, Duarte P, Hu D, Carido M, Sebastião MJ, Gomes-Alves P, Elliott DA, Domian IJ, Teixeira AP, et al. (2018). 3D aggregate culture improves metabolic maturation of human pluripotent stem cell derived cardiomyocytes. Biotechnol. Bioeng. 115, 630–644. [PubMed: 29178315]

Correia C, Koshkin A, Duarte P, Hu D, Teixeira A, Domian I, Serra M, and Alves PM (2017). Distinct carbon sources affect structural and functional maturation of cardiomyocytes derived from human pluripotent stem cells. Sci. Rep. 7, 8590. [PubMed: 28819274]

DeLaughter DM, Bick AG, Wakimoto H, McKean D, Gorham JM, Kathiriya IS, Hinson JT, Homsy J, Gray J, Pu W, et al. (2016). Single-cell resolution of temporal gene expression during heart development. Dev. Cell 39, 480–490. [PubMed: 27840107]

Devalla HD, Schwach V, Ford JW, Milnes JT, El-Haou S, Jackson C, Gkatzis K, Elliott DA, Chuva de Sousa Lopes SM, Mummery CL, et al. (2015). Atrial-like cardiomyocytes from human pluripotent stem cells are a robust preclinical model for assessing atrial-selective pharmacology. EMBO Mol. Med. 7, 394–410. [PubMed: 25700171]

Doulias P-T, Tenopoulou M, Greene JL, Raju K, and Ischiropoulos H (2013). Nitric oxide regulates mitochondrial fatty acid metabolism through reversible protein S-nitrosylation. Sci. Signal. 6, rs1. [PubMed: 23281369]

Dubois NC, Craft AM, Sharma P, Elliott DA, Stanley EG, Elefanty AG, Gramolini A, and Keller G (2011). SIRPA is a specific cell-surface marker for isolating cardiomyocytes derived from human pluripotent stem cells. Nat. Biotechnol. 29, 1011–1018. [PubMed: 22020386]

Elliott DA, Braam SR, Koutsis K, Ng ES, Jenny R, Lagerqvist EL, Biben C, Hatzistavrou T, Hirst CE, Yu QC, et al. (2011). NKX2-5(eGFP/w) hESCs for isolation of human cardiac progenitors and cardiomyocytes. Nat. Methods 8, 1037–1040. [PubMed: 22020065]

Feyen DAM, McKeithan WL, Bruyneel AAN, Spiering S, Hörmann L, Ulmer B, Zhang H, Briganti F, Schweizer M, Hegyi B, et al. (2020). Metabolic maturation media improve physiological function of human iPSC-derived cardiomyocytes. Cell Rep. 32, 107925. [PubMed: 32697997]

Fisher DJ (1984). Oxygenation and metabolism in the developing heart. Semin. Perinatol. 8, 217–225. [PubMed: 6234661]

Fomovsky GM, and Holmes JW (2010). Evolution of scar structure, mechanics, and ventricular function after myocardial infarction in the rat. Am. J. Physiol. Heart Circ. Physiol. 298, H221–H228. [PubMed: 19897714]

Funakoshi S, Fernandes I, Mastikhina O, Wilkinson D, Tran T, Dhahri W, Mazine A, Yang D, Burnett B, Lee J, et al. (2021). Generation of mature compact ventricular cardiomyocytes from human pluripotent stem cells. Nat. Commun. 12, 3155. [PubMed: 34039977]

Gentillon C, Li D, Duan M, Yu W-M, Preininger MK, Jha R, Rampoldi A, Saraf A, Gibson GC, Qu C-K, et al. (2019). Targeting HIF-1a in combination with PPARa activation and postnatal factors promotes the metabolic maturation of human induced pluripotent stem cell-derived cardiomyocytes. J. Mol. Cell. Cardiol. 132, 120–135. [PubMed: 31082397]

Gherghiceanu M, Barad L, Novak A, Reiter I, Itskovitz-Eldor J, Binah O, and Popescu LM (2011). Cardiomyocytes derived from human embryonic and induced pluripotent stem cells: comparative ultrastructure. J. Cell. Mol. Med. 15, 2539–2551. [PubMed: 21883888]

Giacomelli E, Meraviglia V, Campostrini G, Cochrane A, Cao X, van Helden RWJ, Krotenberg Garcia A, Mircea M, Kostidis S, Davis RP, et al. (2020). Human-iPSC-derived cardiac stromal cells enhance maturation in 3D cardiac microtissues and reveal non-cardiomyocyte contributions to heart disease. Cell Stem Cell 26, 862–879.e11. [PubMed: 32459996]

Glatz JFC, Nabben M, Heather LC, Bonen A, and Luiken JJFP (2016). Regulation of the subcellular trafficking of CD36, a major determinant of cardiac fatty acid utilization. Biochim. Biophys. Acta 1861, 1461–1471. [PubMed: 27090938]

Han R, Bansal D, Miyake K, Muniz VP, Weiss RM, McNeil PL, and Campbell KP (2007). Dysferlin-mediated membrane repair protects the heart from stress-induced left ventricular injury. J. Clin. Invest. 117, 1805–1813. [PubMed: 17607357]

Hasenfuss G (1998). Animal models of human cardiovascular disease, heart failure and hypertrophy. Cardiovasc. Res. 39, 60–76. [PubMed: 9764190]

Houser SR, Margulies KB, Murphy AM, Spinale FG, Francis GS, Prabhu SD, Rockman HA, Kass DA, Molkentin JD, Sussman MA, and Koch WJ (2012). Animal models of heart failure: a scientific statement from the American Heart Association. Circ. Res. 111, 131–150. [PubMed: 22595296]

Houten SM, Violante S, Ventura FV, and Wanders RJA (2016). The biochemistry and physiology of mitochondrial fatty acid β-Oxidation and its genetic disorders. Annu. Rev. Physiol. 78, 23–44. [PubMed: 26474213]

Hu D, Linders A, Yamak A, Correia C, Kijlstra JD, Garakani A, Xiao L, Milan DJ, Van Der Meer P, Serra M, et al. (2018). Metabolic maturation of human pluripotent stem cellderived cardiomyocytes by inhibition of HIF1α and LDHA. Circ. Res. 123, 1066–1079. [PubMed: 30355156]

Kamakura T, Makiyama T, Sasaki K, Yoshida Y, Wuriyanghai Y, Chen J, Hattori T, Ohno S, Kita T, Horie M, et al. (2013). Ultrastructural maturation of human-induced pluripotent stem cell-derived cardiomyocytes in a long-term culture. Circ. J. 77, 1307–1314. [PubMed: 23400258]

Karakikes I, Senyei GD, Hansen J, Kong C-W, Azeloglu EU, Stillitano F, Lieu DK, Wang J, Ren L, Hulot JS, et al. (2014). Small molecule-mediated directed differentiation of human embryonic stem cells toward ventricular cardiomyocytes. Stem Cells Transl. Med. 3, 18–31. [PubMed: 24324277]

Karbassi E, Fenix A, Marchiano S, Muraoka N, Nakamura K, Yang X, and Murry CE (2020). Cardiomyocyte maturation: advances in knowledge and implications for regenerative medicine. Nat. Rev. Cardiol. 17, 341–359. [PubMed: 32015528]

Kattman SJ, Witty AD, Gagliardi M, Dubois NC, Niapour M, Hotta A, Ellis J, and Keller G (2011). Stage-specific optimization of activin/nodal and BMP signaling promotes cardiac differentiation of mouse and human pluripotent stem cell lines. Cell Stem Cell 8, 228–240. [PubMed: 21295278]

Kliewer SA, Forman BM, Blumberg B, Ong ES, Borgmeyer U, Mangelsdorf DJ, Umesono K, and Evans RM (1994). Differential expression and activation of a family of murine peroxisome proliferator-activated receptors. Proc. Natl. Acad. Sci. USA 91, 7355–7359. [PubMed: 8041794]

Kosmidis G, Bellin M, Ribeiro MC, van Meer B, Ward-van Oostwaard D, Passier R, Tertoolen LGJ, Mummery CL, and Casini S (2015). Altered calcium handling and increased contraction

force in human embryonic stem cell derived cardiomyocytes following short term dexamethasone exposure. Biochem. Biophys. Res. Commun. 467, 998–1005. [PubMed: 26456652]

Lee JH, Protze SI, Laksman Z, Backx PH, and Keller GM (2017a). Human pluripotent stem cell-derived atrial and ventricular cardiomyocytes develop from distinct mesoderm populations. Cell Stem Cell 21, 179–194.e4. [PubMed: 28777944]

Lee S, Serpooshan V, Tong X, Venkatraman S, Lee M, Lee J, Chirikian O, Wu JC, Wu SM, and Yang F (2017b). Contractile force generation by 3D hiPSC-derived cardiac tissues is enhanced by rapid establishment of cellular interconnection in matrix with muscle-mimicking stiffness. Biomaterials 131, 111–120. [PubMed: 28384492]

Lee WS, and Kim J (2015). Peroxisome proliferator-activated receptors and the heart: lessons from the past and future directions. PPAR Res. 2015, 271983. [PubMed: 26587015]

Lemoine MD, Mannhardt I, Breckwoldt K, Prondzynski M, Flenner F, Ulmer B, Hirt MN, Neuber C, Horváth A, Kloth B, et al. (2017). Human iPSC-derived cardiomyocytes cultured in 3D engineered heart tissue show physiological upstroke velocity and sodium current density. Sci. Rep. 7, 5464. [PubMed: 28710467]

Leonard A, Bertero A, Powers JD, Beussman KM, Bhandari S, Regnier M, Murry CE, and Sniadecki NJ (2018). Afterload promotes maturation of human induced pluripotent stem cell derived cardiomyocytes in engineered heart tissues. J. Mol. Cell. Cardiol. 118, 147–158. [PubMed: 29604261]

Lex A, Gehlenborg N, Strobelt H, Vuillemot R, and Pfister H (2014). UpSet: visualization of intersecting sets. IEEE Trans. Vis. Comput. Graph. 20, 1983–1992. [PubMed: 26356912]

Li RA, Keung W, Cashman TJ, Backeris PC, Johnson BV, Bardot ES, Wong AOT, Chan PKW, Chan CWY, and Costa KD (2018). Bioengineering an electro-mechanically functional miniature ventricular heart chamber from human pluripotent stem cells. Biomaterials 163, 116–127. [PubMed: 29459321]

Lian X, Hsiao C, Wilson G, Zhu K, Hazeltine LB, Azarin SM, Raval KK, Zhang J, Kamp TJ, and Palecek SP (2012). Robust cardiomyocyte differentiation from human pluripotent stem cells via temporal modulation of canonical Wnt signaling. Proc. Natl. Acad. Sci. USA 109, E1848–E1857. [PubMed: 22645348]

Lian X, Zhang J, Azarin SM, Zhu K, Hazeltine LB, Bao X, Hsiao C, Kamp TJ, and Palecek SP (2013). Directed cardiomyocyte differentiation from human pluripotent stem cells by modulating Wnt/beta-catenin signaling under fully defined conditions. Nat. Protoc. 8, 162–175. [PubMed: 23257984]

Liu A, Tang M, Xi J, Gao L, Zheng Y, Luo H, Hu X, Zhao F, Reppel M, Hescheler J, and Liang H (2010). Functional characterization of inward rectifier potassium ion channel in murine fetal ventricular cardiomyocytes. Cell. Physiol. Biochem. 26, 413–420. [PubMed: 20798526]

Liu J, Wang P, He L, Li Y, Luo J, Cheng L, Qin Q, Brako LA, Lo WK, Lewis W, Yang Q, et al. (2011). Cardiomyocyte-restricted deletion of PPARβ/δ in PPARα-null mice causes impaired mitochondrial biogenesis and defense, but no further depression of myocardial fatty acid oxidation. PPAR Res. 2011, 372854. [PubMed: 21904539]

Lopaschuk GD, and Jaswal JS (2010). Energy metabolic phenotype of the cardiomyocyte during development, differentiation, and postnatal maturation. J. Cardiovasc. Pharmacol. 56, 130–140. [PubMed: 20505524]

Lopez CA, Al-Siddiqi HHAA, Purnama U, Iftekhar S, Bruyneel AAN, Kerr M, Nazir R, da Luz Sousa Fialho M, Malandraki-Miller S, Alonaizan R, et al. (2021). Physiological and pharmacological stimulation for in vitro maturation of substrate metabolism in human induced pluripotent stem cell-derived cardiomyocytes. Sci. Rep. 11, 7802. [PubMed: 33833285]

Lund J, Aas V, Tingstad RH, Van Hees A, and Nikolić N (2018). Utilization of lactic acid in human myotubes and interplay with glucose and fatty acid metabolism. Sci. Rep. 8, 9814. [PubMed: 29959350]

Mannhardt I, Saleem U, Benzin A, Schulze T, Klampe B, Eschenhagen T, and Hansen A (2017). Automated contraction analysis of human engineered heart tissue for cardiac drug safety screening. J. Vis. Exp. 122, 55461.

Menendez-Montes I, Escobar B, Palacios B, Gómez MJ, Izquierdo-Garcia JL, Flores L, Jiménez-Borreguero LJ, Aragones J, Ruiz-Cabello J, Torres M, and Martin-Puig S (2016). Myocardial VHL-HIF signaling controls an embryonic metabolic switch essential for cardiac maturation. Dev. Cell 39, 724–739. [PubMed: 27997827]

Mills RJ, Titmarsh DM, Koenig X, Parker BL, Ryall JG, Quaife-Ryan GA, Voges HK, Hodson MP, Ferguson C, Drowley L, et al. (2017). Functional screening in human cardiac organoids reveals a metabolic mechanism for cardiomyocyte cell cycle arrest. Proc. Natl. Acad. Sci. USA 114, E8372–E8381. [PubMed: 28916735]

Murphy SA, Miyamoto M, Kervadec A, Kannan S, Tampakakis E, Kambhampati S, Lin BL, Paek S, Andersen P, Lee D-I, et al. (2021). PGC1/PPAR drive cardiomyocyte maturation at single cell level via YAP1 and SF3B2. Nat. Commun. 12, 1648. [PubMed: 33712605]

Murry CE, and Keller G (2008). Differentiation of embryonic stem cells to clinically relevant populations: lessons from embryonic development. Cell 132, 661–680. [PubMed: 18295582]

Naito AT, Shiojima I, Akazawa H, Hidaka K, Morisaki T, Kikuchi A, and Komuro I (2006). Developmental stage-specific biphasic roles of Wnt/β-catenin signaling in cardiomyogenesis and hematopoiesis. Proc. Natl. Acad. Sci. USA 103, 19812–19817. [PubMed: 17170140]

Nakano H, Minami I, Braas D, Pappoe H, Wu X, Sagadevan A, Vergnes L, Fu K, Morselli M, Dunham C, et al. (2017). Glucose inhibits cardiac muscle maturation through nucleotide biosynthesis. Elife 6, e29330. [PubMed: 29231167]

Neely JR, and Morgan HE (1974). Relationship between carbohydrate and lipid metabolism and the energy balance of heart muscle. Annu. Rev. Physiol. 36, 413–459. [PubMed: 19400669]

Nunes SS, Miklas JW, Liu J, Aschar-Sobbi R, Xiao Y, Zhang B, Jiang J, Massé S, Gagliardi M, Hsieh A, et al. (2013). Biowire: a platform for maturation of human pluripotent stem cell-derived cardiomyocytes. Nat. Methods 10, 781–787. [PubMed: 23793239]

Paige SL, Galdos FX, Lee S, Chin ET, Ranjbarvaziri S, Feyen DAM, Darsha AK, Xu S, Ryan JA, Beck AL, et al. (2020). Patient-specific induced pluripotent stem cells implicate intrinsic impaired contractility in hypoplastic left heart syndrome. Circulation 142, 1605–1608. [PubMed: 33074758]

Parikh SS, Blackwell DJ, Gomez-Hurtado N, Frisk M, Wang L, Kim K, Dahl CP, Fiane A, Tønnessen T, Kryshtal DO, et al. (2017). Thyroid and glucocorticoid hormones promote functional T-tubule development in human-induced pluripotent stem cell–derived cardiomyocytes. Circ. Res. 121, 1323–1330. [PubMed: 28974554]

Pavlovic BJ, Blake LE, Roux J, Chavarria C, and Gilad Y (2018). A comparative assessment of human and chimpanzee iPSC-derived cardiomyocytes with primary heart tissues. Sci. Rep. 8, 15312. [PubMed: 30333510]

Péterfi Z, Tóth ZE, Kovács HA, Lázár E, Sum A, Donkó A, Sirokmány G, Shah AM, and Geiszt M (2014). Peroxidasin-like protein: a novel peroxidase homologue in the human heart. Cardiovasc. Res. 101, 393–399. [PubMed: 24253521]

Piquereau J, and Ventura-Clapier R (2018). Maturation of cardiac energy metabolism During perinatal development. Front. Physiol. 9, 959. [PubMed: 30072919]

Poon E, Keung W, Liang Y, Ramalingam R, Yan B, Zhang S, Chopra A, Moore J, Herren A, Lieu DK, et al. (2015). Proteomic analysis of human pluripotent stem cell-derived, fetal, and adult ventricular cardiomyocytes reveals pathways crucial for cardiac metabolism and maturation. Circ. Cardiovasc. Genet. 8, 427–436. [PubMed: 25759434]

Poon EN-Y, Luo XL, Webb SE, Yan B, Zhao R, Wu SCM, Yang Y, Zhang P, Bai H, Shao J, et al. (2020). The cell surface marker CD36 selectively identifies matured, mitochondria-rich hPSC-cardiomyocytes. Cell Res. 30, 626–629. [PubMed: 32157205]

Ronaldson-Bouchard K, Ma SP, Yeager K, Chen T, Song LJ, Sirabella D, Morikawa K, Teles D, Yazawa M, and Vunjak-Novakovic G (2018). Advanced maturation of human cardiac tissue grown from pluripotent stem cells. Nature 556, 239–243. [PubMed: 29618819]

Ruan JL, Tulloch NL, Razumova MV, Saiget M, Muskheli V, Pabon L, Reinecke H, Regnier M, and Murry CE (2016). Mechanical stress conditioning and electrical stimulation promote contractility and force maturation of induced pluripotent stem cell-derived human cardiac tissue. Circulation 134, 1557–1567. [PubMed: 27737958]

Schaaf S, Eder A, Vollert I, Stöhr A, Hansen A, and Eschenhagen T (2014). Generation of strip-format fibrin-based engineered heart tissue (EHT). In Cardiac Tissue Engineering: Methods and Protocols, Radisic M and Black LD III, eds. (Springer), pp. 121–129.

Schaniel C, Dhanan P, Hu B, Xiong Y, Raghunandan T, Gonzalez DM, Dariolli R, D'Souza SL, Yadaw AS, Hansen J, et al. (2021). A library of induced pluripotent stem cells from clinically well-characterized, diverse healthy human individuals. Stem Cell Rep. 16, 3036–3049.

Schindelin J, Arganda-Carreras I, Frise E, Kaynig V, Longair M, Pietzsch T, Preibisch S, Rueden C, Saalfeld S, Schmid B, et al. (2012). Fiji: an open-source platform for biological-image analysis. Nat. Methods 9, 676–682. [PubMed: 22743772]

Serpooshan V, Chen P, Wu H, Lee S, Sharma A, Hu DA, Venkatraman S, Ganesan AV, Usta OB, Yarmush M, et al. (2017). Bioacoustic-enabled patterning of human iPSC-derived cardiomyocytes into 3D cardiac tissue. Biomaterials 131, 47–57. [PubMed: 28376365]

Serrao GW, Turnbull IC, Ancukiewicz D, Kim DE, Kao E, Cashman TJ, Hadri L, Hajjar RJ, and Costa KD (2012). Myocyte-depleted engineered cardiac tissues support therapeutic potential of mesenchymal stem cells. Tissue Eng. Part A 18, 1322–1333. [PubMed: 22500611]

Shadrin IY, Allen BW, Qian Y, Jackman CP, Carlson AL, Juhas ME, and Bursac N (2017). Cardiopatch platform enables maturation and scale-up of human pluripotent stem cell-derived engineered heart tissues. Nat. Commun. 8, 1825. [PubMed: 29184059]

Shearer BG, Steger DJ, Way JM, Stanley TB, Lobe DC, Grillot DA, Iannone MA, Lazar MA, Willson TM, and Billin AN (2008). Identification and characterization of a selective peroxisome proliferator-activated receptor beta/delta (NR1C2) antagonist. Mol. Endocrinol. 22, 523–529. [PubMed: 17975020]

Shimozawa N, Tsukamoto T, Suzuki Y, Orii T, Shirayoshi Y, Mori T, and Fujiki Y (1992). A human gene responsible for Zellweger syndrome that affects peroxisome assembly. Science 255, 1132–1134. [PubMed: 1546315]

Skelton RJP, Costa M, Anderson DJ, Bruveris F, Finnin BW, Koutsis K, Arasaratnam D, White AJ, Rafii A, Ng ES, et al. (2014). SIRPA, VCAM1 and CD34 identify discrete lineages during early human cardiovascular development. Stem Cell Res. 13, 172–179. [PubMed: 24968096]

Slaats RH, Schwach V, and Passier R (2020). Metabolic environment in vivo as a blueprint for differentiation and maturation of human stem cell-derived cardiomyocytes. Biochim. Biophys. Acta Mol. Basis Dis. 1866, 165881. [PubMed: 32562698]

Stanley WC, Recchia FA, and Lopaschuk GD (2005). Myocardial substrate metabolism in the normal and failing heart. Physiol. Rev. 85, 1093–1129. [PubMed: 15987803]

Sznaidman ML, Haffner CD, Maloney PR, Fivush A, Chao E, Goreham D, Sierra ML, LeGrumelec C, Xu HE, Montana VG, et al. (2003). Novel selective small molecule agonists for peroxisome proliferator-activated receptor delta (PPARdelta)—synthesis and biological activity. Bioorg. Med. Chem. Lett. 13, 1517–1521. [PubMed: 12699745]

Thavandiran N, Dubois N, Mikryukov A, Massé S, Beca B, Simmons CA, Deshpande VS, McGarry JP, Chen CS, Nanthakumar K, et al. (2013). Design and formulation of functional pluripotent stem cell-derived cardiac microtissues. Proc. Natl. Acad. Sci. USA 110, E4698–E4707. [PubMed: 24255110]

Tiburcy M, Didié M, Boy O, Christalla P, Döker S, Naito H, Karikkineth BC, El-Armouche A, Grimm M, Nose M, et al. (2011). Terminal differentiation, advanced organotypic maturation, and modeling of hypertrophic growth in engineered heart tissue. Circ. Res. 109, 1105–1114. [PubMed: 21921264]

Tiburcy M, Hudson JE, Balfanz P, Schlick SF, Meyer T, Chang Liao M-L, Levent E, Raad F, Zeidler S, Wingender E, et al. (2017). Defined engineered human myocardium with advanced maturation for applications in heart failure modeling and repair. Circulation 135, 1832–1847. [PubMed: 28167635]

Tohyama S, Hattori F, Sano M, Hishiki T, Nagahata Y, Matsuura T, Hashimoto H, Suzuki T, Yamashita H, Satoh Y, et al. (2013). Distinct metabolic flow enables large-scale purification of mouse and human pluripotent stem cell-derived cardiomyocytes. Cell Stem Cell 12, 127–137. [PubMed: 23168164]

Tomec RJ, and Hoppel CL (1975). Carnitine palmitoyltransferase in bovine fetal heart mitochondria. Arch. Biochem. Biophys. 170, 716–723. [PubMed: 1190787]

Tsang HG, Rashdan NA, Whitelaw CBA, Corcoran BM, Summers KM, and MacRae VE (2016). Large animal models of cardiovascular disease. Cell Biochem. Funct. 34, 113–132. [PubMed: 26914991]

Turnbull IC, Karakikes I, Serrao GW, Backeris P, Lee J-J, Xie C,Senyei G, Gordon RE, Li RA, Akar FG, et al. (2014). Advancing functional engineered cardiac tissues toward a preclinical model of human myocardium. FASEB J. 28, 644–654. [PubMed: 24174427]

Turnbull IC, Mayourian J, Murphy JF, Stillitano F, Ceholski DK, and Costa KD (2018). Cardiac tissue engineering models of inherited and acquired cardiomyopathies. Methods Mol. Biol. 1816, 145–159. [PubMed: 29987817]

Ueno S, Weidinger G, Osugi T, Kohn AD, Golob JL, Pabon L, Reinecke H, Moon RT, and Murry CE (2007). Biphasic role for Wnt/β-cat-enin signaling in cardiac specification in zebrafish and embryonic stem cells. Proc. Natl. Acad. Sci. USA 104, 9685–9690. [PubMed: 17522258]

Ulmer BM, and Eschenhagen T (2020). Human pluripotent stem cell-derived cardiomyocytes for studying energy metabolism. Biochim. Biophys. Acta Mol. Cell Res. 1867, 118471. [PubMed: 30954570]

Ulmer BM, Stoehr A, Schulze ML, Patel S, Gucek M, Mannhardt I, Funcke S, Murphy E, Eschenhagen T, and Hansen A (2018). Contractile work contributes to maturation of energy metabolism in hiPSC-derived cardiomyocytes. Stem Cell Rep. 10, 834–847.

Uosaki H, Cahan P, Lee DI, Wang S, Miyamoto M, Fernandez L, Kass DA, and Kwon C (2015). Transcriptional landscape of cardiomyocyte maturation. Cell Rep. 13, 1705–1716. [PubMed: 26586429]

van den Berg CW, Okawa S, Chuva de Sousa Lopes SM, van Iperen L, Passier R, Braam SR, Tertoolen LG, del Sol A, Davis RP, and Mummery CL (2015). Transcriptome of human foetal heart compared with cardiomyocytes from pluripotent stem cells. Development 142, 3231–3238. [PubMed: 26209647]

Virani SS, Alonso A, Benjamin EJ, Bittencourt MS, Callaway CW, Carson AP, Chamberlain AM, Chang AR, Cheng S, Delling FN, et al. (2020). Heart disease and stroke Statistics-2020 update: a report from the American Heart Association. Circulation 141, e139–e596. [PubMed: 31992061]

Vora S, Seaman C, Durham S, and Piomelli S (1980). Isozymes of human phosphofructokinase: identification and subunit structural characterization of a new system. Proc. Natl. Acad. Sci. USA 77, 62–66. [PubMed: 6444721]

Warshaw JB, and Terry ML (1970). Cellular energy metabolism during fetal development. II. Fatty acid oxidation by the developing heart. J. Cell Biol. 44, 354–360. [PubMed: 5415033]

Werner JC, and Sicard RE (1987). Lactate metabolism of isolated, perfused fetal, and newborn pig hearts. Pediatr. Res. 22, 552–556. [PubMed: 3684382]

Werner JC, Whitman V, Vary TC, Fripp RR, Musselman J, and Schuler HG (1983). Fatty acid and glucose utilization in isolated, working newborn pig hearts. Am. J. Physiol. 244, E19–E23. [PubMed: 6849379]

Wittels B, and Bressler R (1965). Lipid metabolism in the newborn heart. J. Clin. Invest. 44, 1639–1646. [PubMed: 5840533]

Xu F, Chen Y, Tillman KA, Cui Y, Williams RW, Bhattacharya SK, Lu L, and Sun Y (2021). Characterizing modifier genes of cardiac fibrosis phenotype in hypertrophic cardiomyopathy. Int. J. Cardiol. 330, 135–141. [PubMed: 33529666]

Yang L, Soonpaa MH, Adler ED, Roepke TK, Kattman SJ, Kennedy M, Henckaerts E, Bonham K, Abbott GW, Linden RM, et al. (2008). Human cardiovascular progenitor cells develop from a KDR+ embryonic-stem-cell-derived population. Nature 453, 524–528. [PubMed: 18432194]

Yang X, Pabon L, and Murry CE (2014a). Engineering adolescence: maturation of human pluripotent stem cell-derived cardiomyocytes. Circ. Res. 114, 511–523. [PubMed: 24481842]

Yang X, Rodriguez M, Pabon L, Fischer KA, Reinecke H, Regnier M, Sniadecki NJ, Ruohola-Baker H, and Murry CE (2014b). Tri-iodo-l-thyronine promotes the maturation of human cardiomyocytes-derived from induced pluripotent stem cells. J. Mol. Cell. Cardiol. 72, 296–304. [PubMed: 24735830]

Yang X, Rodriguez ML, Leonard A, Sun L, Fischer KA, Wang Y, Ritterhoff J, Zhao L, Kolwicz SCJ, Pabon L, et al. (2019). Fatty acids enhance the maturation of cardiomyocytes derived from human pluripotent stem cells. Stem Cell Rep. 13, 657–668.

Zhang J, Klos M, Wilson GF, Herman AM, Lian X, Raval KK, Barron MR, Hou L, Soerens AG, Yu J, et al. (2012). Extracellular matrix promotes highly efficient cardiac differentiation of human pluripotent stem cells: the matrix sandwich method. Circ. Res. 111, 1125–1136. [PubMed: 22912385]

Zhang Q, Jiang J, Han P, Yuan Q, Zhang J, Zhang X, Xu Y, Cao H, Meng Q, Chen L, et al. (2011). Direct differentiation of atrial and ventricular myocytes from human embryonic stem cells by alternating retinoid signals. Cell Res. 21, 579–587. [PubMed: 21102549]

Zhao Y, Rafatian N, Wang EY, Feric NT, Lai BFL, Knee-Walden EJ, Backx PH, and Radisic M (2020). Engineering microenvironment for human cardiac tissue assembly in heart-on-a-chip platform. Matrix Biol. 85–86, 189–204.

Highlights

- PPARd signaling demonstrates isoform-specific effects on hPSC-derived cardiomyocytes
- PPARd activation increases sarcomere alignment, cell size, and multinuclear cells
- PPARd activation induces a metabolic shift from glycolysis to FAO
- Transient lactate exposure induces maturation in hPSC-derived cardiomyocytes

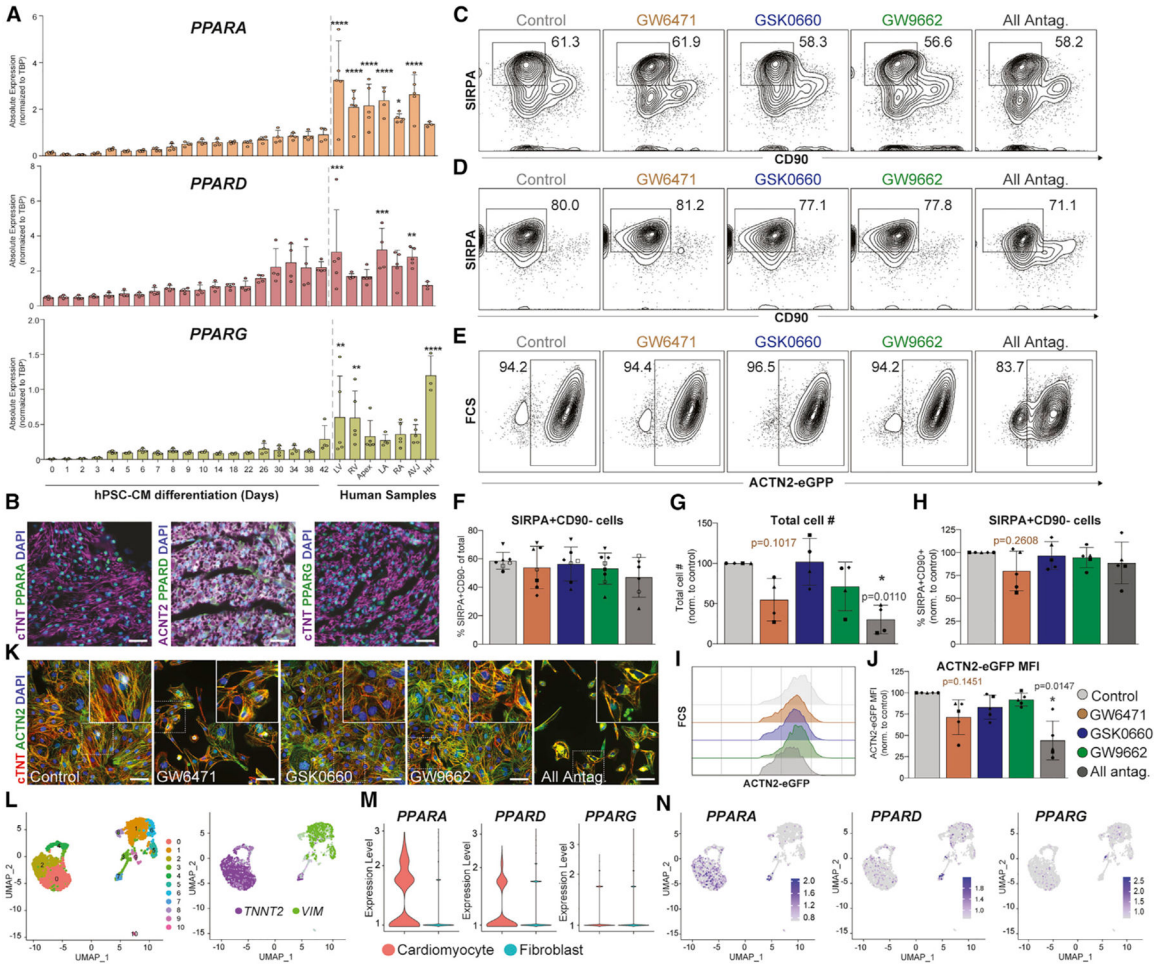

Figure 1. PPAR isoforms show distinct expression and function during hPSC-CM differentiation and maturation

(A) RT-qPCR analysis of *PPARA*, *PPARD*, and *PPARG* during hPSC-CM differentiation (n = 4) and in human fetal heart tissue (week 16 of gestation).

(B) Composite IF images for cardiac troponin T (cTnT) or alpha-actinin (ACNT2) in combination with PPARa, PPARd, or PPARg on week 16 human fetal heart (left ventricle). DAPI is used to visualize nuclei. Scale bars: 25 μm.

(C) Flow cytometry analysis of hPSC-CMs at day 20 of differentiation for SIRPA and CD90.

(D and E) Flow cytometry analysis of hPSC-CMs at day 35 of differentiation for SIRPA and CD90 or for ACTN2-eGFP. Cells were treated with PPAR antagonists for 2 weeks prior to analysis.

(F) Quantification of SIRPA+CD90— hPSC-CMs from (C).

(G) Quantification of total cell numbers from (C).

(H) Quantification of SIRPA+CD90— hPSC-CMs from (D).

(I) ACTN2-eGFP fluorescence intensity in hPSC-CMs treated with PPAR antagonists for 2 weeks (days 20–35).

(J) Quantification of ACTN2-eGFP mean fluorescence intensity in (I).

(K) Composite IF images for cTnT and ACTN2 in hPSC-CMs treated with PPAR antagonists for 2 weeks (days 20–35). DAPI is used to visualize nuclei. Scale bars: 50 μm.

(L) ScRNA-seq UMAP clustering of hPSC-CMs (left) and expression of cTnT (green) and vimentin (purple) (right).

(M) cTnT+ (red) and Vimentin+ (blue) cells were grouped, and expression of PPAR isoforms assessed.

(N) Expression of *PPARA*, *PPARD*, and *PPARG* in hPSC-CMs. Biological replicates are identified by same shape of respective data points.

Data represented as mean ± SD. Statistics: Student's t tests relative to control (far left) (*p < 0.05; **p < 0.01; ***p < 0.001; **** p < 0.0001). AVJ, atrioventricular junction; HH, human heart (adult); LA, left atria; LV, left ventricle; RA, right atrial; RV, right ventricle.

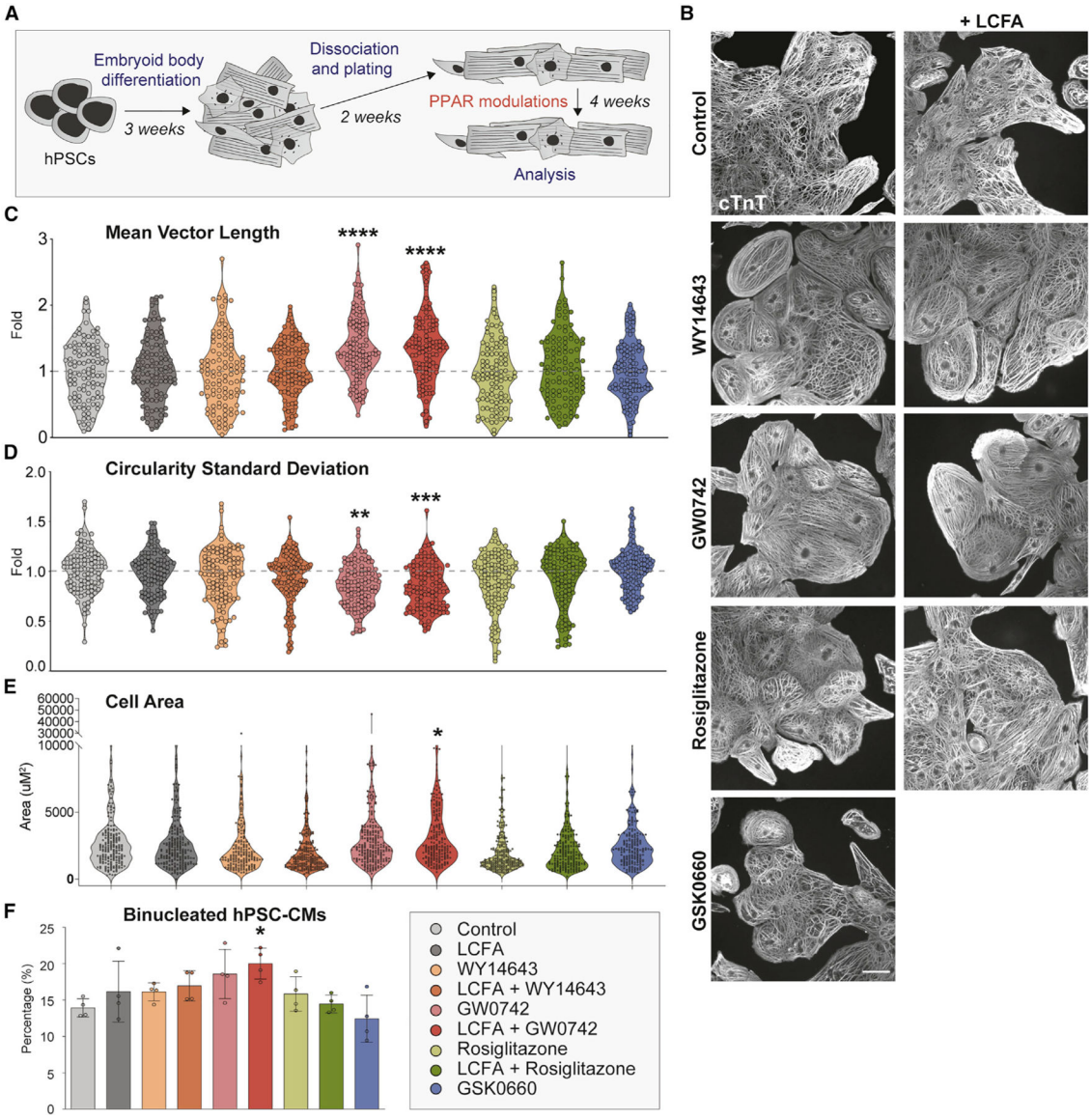

Figure 2. PPARd activation induces changes in cell morphology, cell size, and number of nuclei in hPSC-CMs

(A) Schematic of experimental outline.

(B) IF analysis for cTnT 4 weeks after PPAR modulations. Representative images are shown, scale bars: 50 μm.

(C and D) Mean vector length and circularity standard deviation quantified by MatFiber from IF analysis images for cTnT (n = 3, >15 hPSC-CMs/biological replicate).

(E) Cell surface area measured on images from IF analysis for ACTN2 (n = 3, >15 hPSC-CMs/biological replicate).

(F) Percentage of binucleated hPSC-CMs determined on images from IF analysis for ACTN2 and DAPI stain (n = 4, >250 hPSC-CMs/condition).

Data represented as mean ± SD. Statistics: one-way ANOVA and Tukey test for multiple comparisons (*p ≤ 0.05; **p ≤ 0.01); ***p ≤ 0.001; **** p ≤ 0.0001) relative to control (far left).

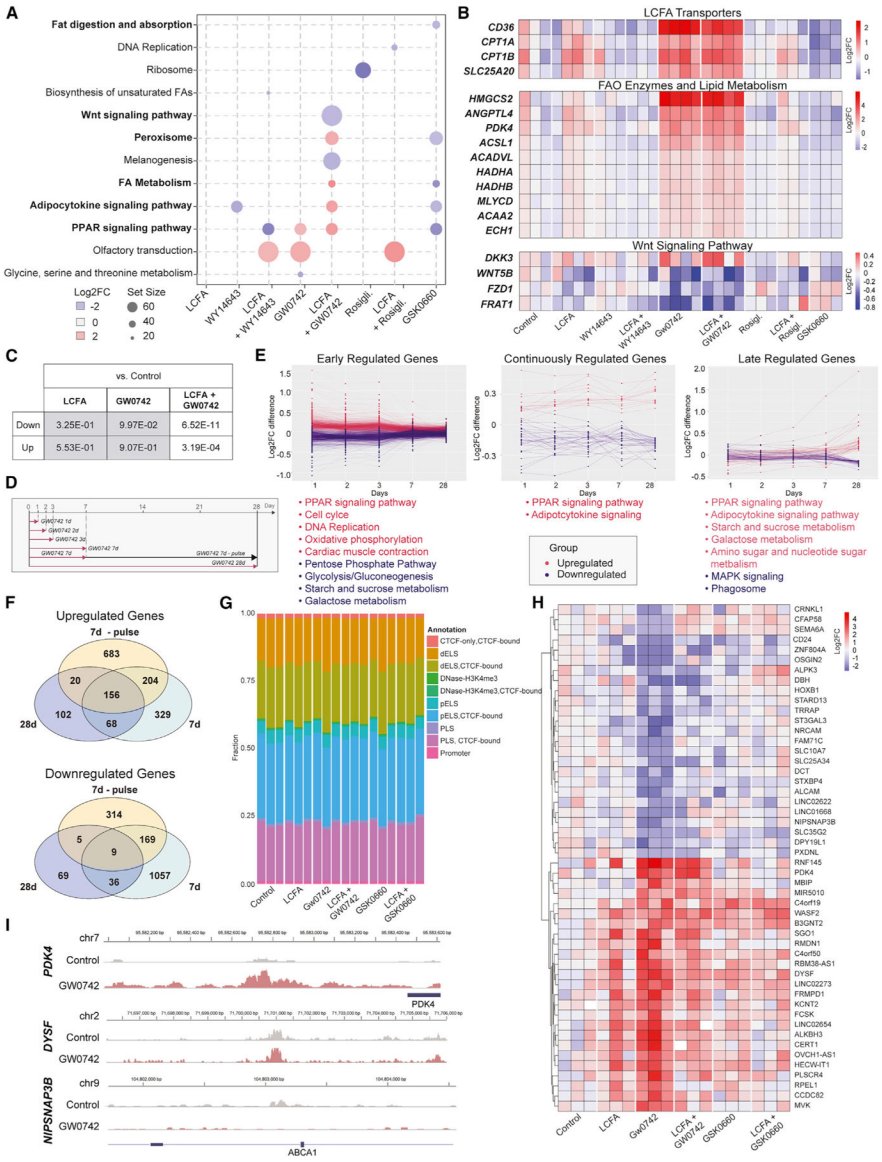

Figure 3. PPARd activates the FAO transcriptional program in hPSC-CMs

(A) Comparison of KEGG pathways differentially regulated in PPAR modulated hPSC-CMs compared with control 4 weeks after continuous PPAR modulation (set size−number of genes from KEGG pathway in dataset).

(B) Expression of key candidates involved in FAO.

(C) Genes differentially expressed in PPARd-modulated compared with control hPSC-CMs with gene sets of differentially expressed genes between D27 hPSC-CMs and the adult heart (Pavlovic et al., 2018).

(D) Schematic of PPARd modulations and hPSC-CM harvest time points.

(E) Temporal analysis of gene expression changes reveals significantly regulated genes only on days 1, 2, 3, and 7 (left), changed at all time points (middle), and regulated late (right).

(F) Venn diagram of upregulated (top) and downregulated (bottom) genes after 7 days, a 7-day pulse, and 28 days of PPARd activation compared with control.

(G) Stacked bar chart of the promoter- and enhancer-associated peaks identified by ATAC-seq.

(H) Heatmap of 50 genes with the greatest differential chromatin accessibility (25 most increased accessibility; 25 most decreased accessibility) between control and PPARd-activated hPSC-CMs.

(I) ATAC-seq tracks for *PDK4*, *DYSF*, and *NIPSNAP3B*.

Statistics: DESeq2 was used to normalize read counts and determine differentially expressed genes with $p < 0.05$ relative to control (far left).

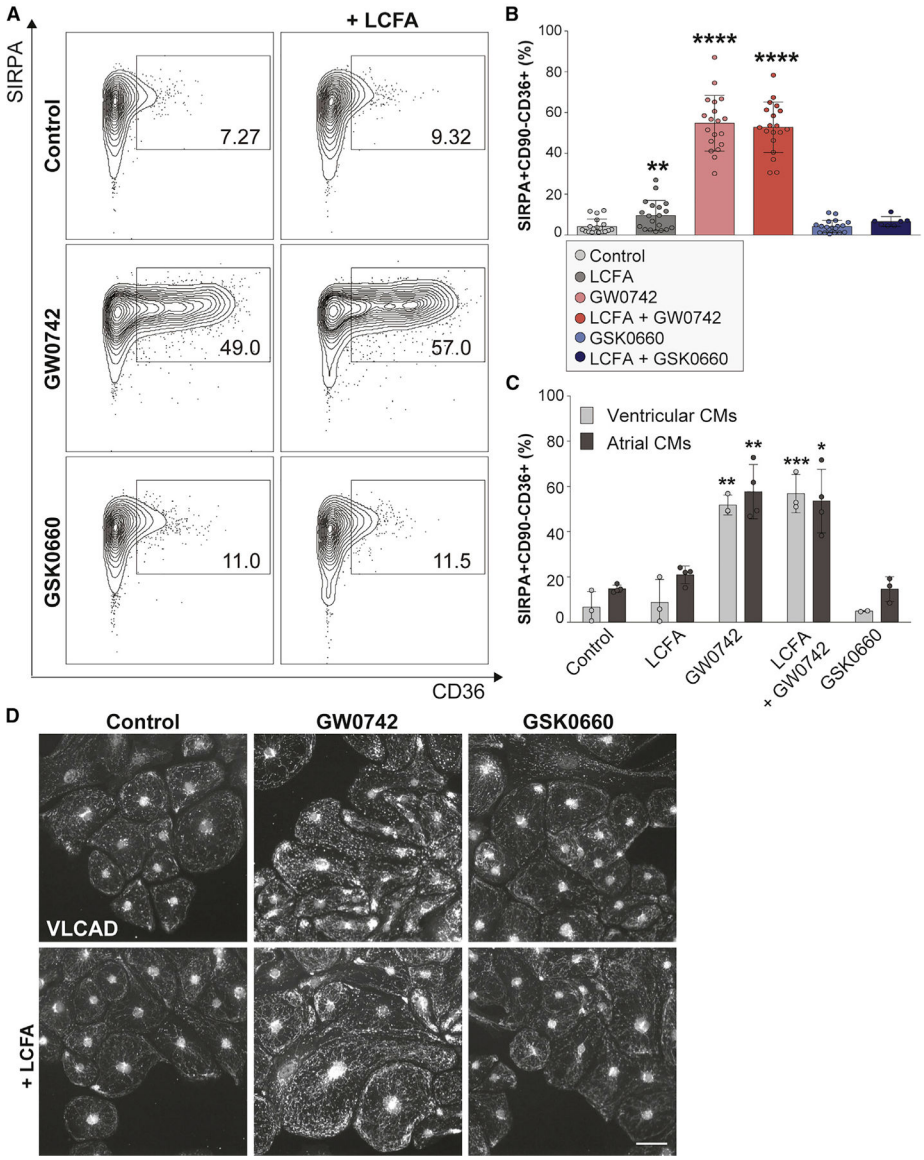

Figure 4. PPARd activation induces key FAO components in ventricular and atrial hPSC-CMs

(A) Flow cytometry analysis 4 weeks after continuous PPAR modulations.

(B) Quantification from (A), (n = 7–19 biological replicates).

(C) Flow-cytometry analysis of CD36 expression after PPAR modulation in ventricular and atrial hPSC-CMs (n = 2–4).

(D) IF analysis for VLCAD 4 weeks after continuous PPAR modulation. Scale bars, 50 μm. Data represented as mean ± SD. Statistics: Student's t tests relative to control (far left) (*p < 0.05; **p < 0.01; ***p < 0.001; ****p < 0.0001).

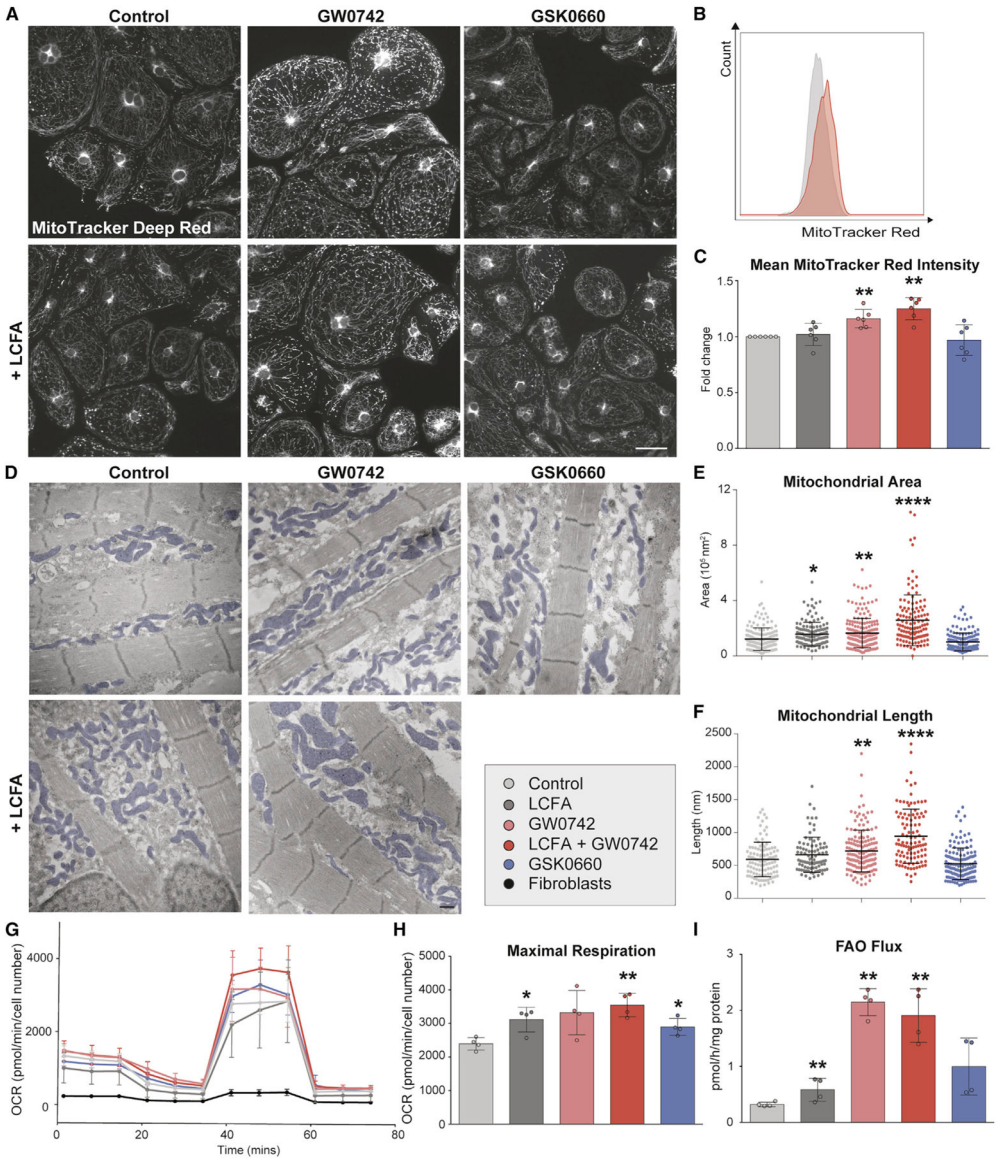

Figure 5. PPARd activation induces mitochondrial maturation and FAO in hPSC-CMs

(A) MitoTracker Deep Red dye analysis 4 weeks after continuous PPARd modulations. Scale bars: 50 μm.

(B and C) Mitochondrial content quantification by MitoTracker Deep Red flow cytometry. Representative flow cytometry plots for control and LCFA + GW0742 treated hPSC-CMs (B) and quantification in all conditions (C) (n = 6).

(D) TEM analysis 4 weeks after continuous PPARd modulations. Mitochondria pseudo-colored in blue. Scale bars: 500 nm.

(E and F) Quantification of mitochondrial area and length on TEM images. Data collected from 5–10 images per conditions, with a minimum of 10 mitochondria per image.

(G and H) Oxygen consumption rate (OCR) in hPSC-CMs and hPSC-derived fibroblasts (black) 4 weeks after continuous PPARd modulations (n = 4; n = 5–8 technical replicates/condition; normalized to cell number).

(I) FAO flux assay 4 weeks after PPARd modulation (n = 4).

Data represented as mean ± SD. Statistics: (C, H, and I) Student's t tests (*p < 0.05; **p < 0.01; ***p < 0.001; **** p < 0.0001) relative to control (far left). (E and F) One-way ANOVA and Tukey test for multiple comparisons (*p ≤ 0.05; **p ≤ 0.01); ***p ≤ 0.001; ****p ≤ 0.0001) relative to control (far left).

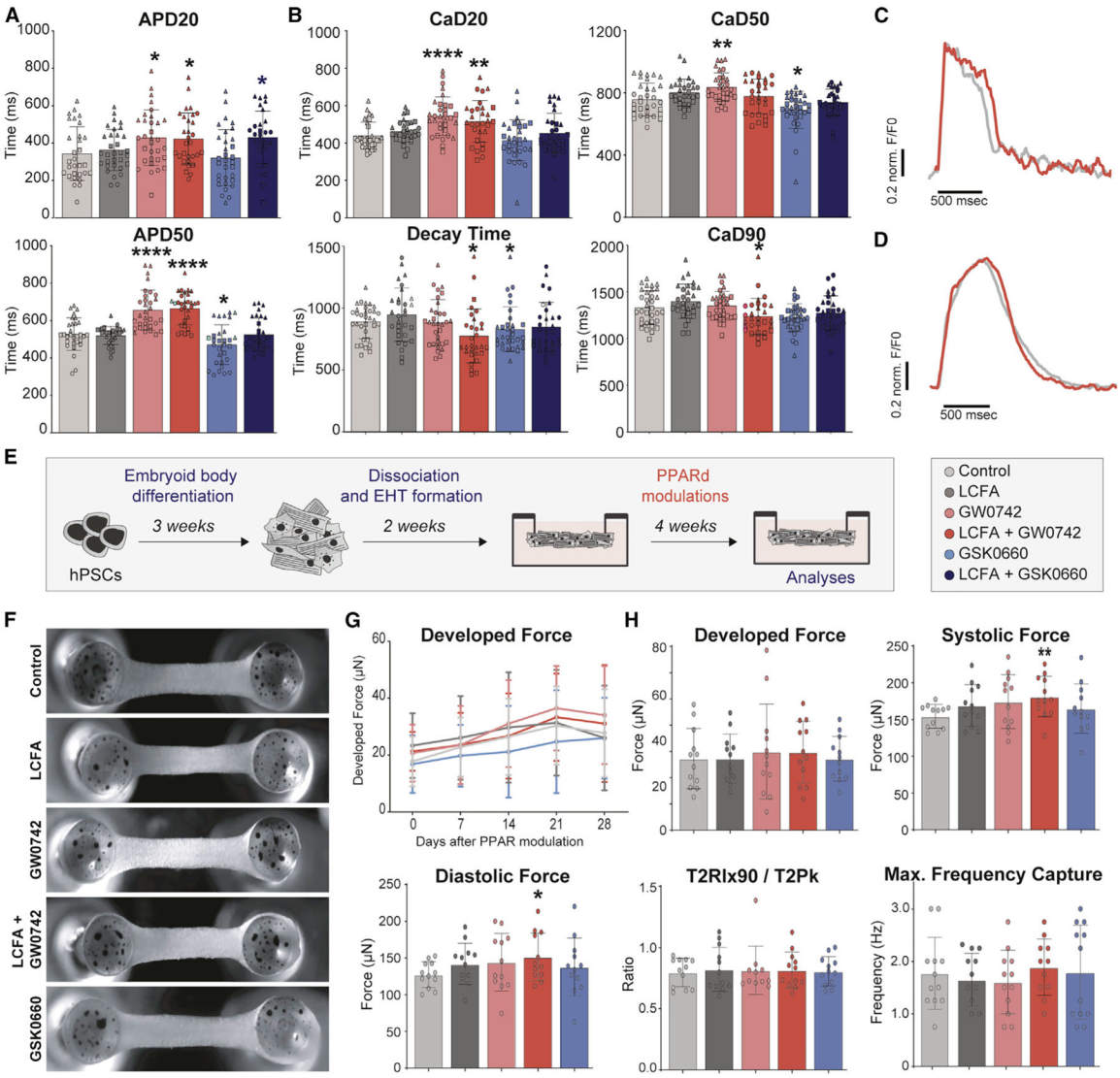

Figure 6. PPARd activation improves hPSC-CM electrophysiological and contractile maturation

(A and B) Action potential (AP) measurements (A) and calcium transient analysis (B) on single hPSC-CMs 4 weeks after continuous PPARd activation or inhibition, paced at 0.5 Hz (n = 3 biological replicates, 4–10 hPSC-CMs measured/condition/replicate).

(C and D) Representative AP (C) and calcium transients (D) traces of control and LCFA + GW0742 treated hPSC-CMs.

(E) Schematic of experimental outline for EHT analysis.

(F) Brightfield images of EHTs 4 weeks after PPAR modulation.

(G) Contractile force measurements in spontaneously contracting EHTs during the 4 weeks of continuous PPARd modulations.

(H) Analyses of EHTs 4 weeks after continuous PPARd modulations. EHTs were paced at 1.0 Hz (n = 4; 3 EHTs/biological replicate). Biological replicates identified by same shape of respective data points.

Data represented as mean ± SD. Statistics: Student's t tests relative to control (far left) (*p < 0.05; **p < 0.01; ***p < 0.001; **** p < 0.0001).

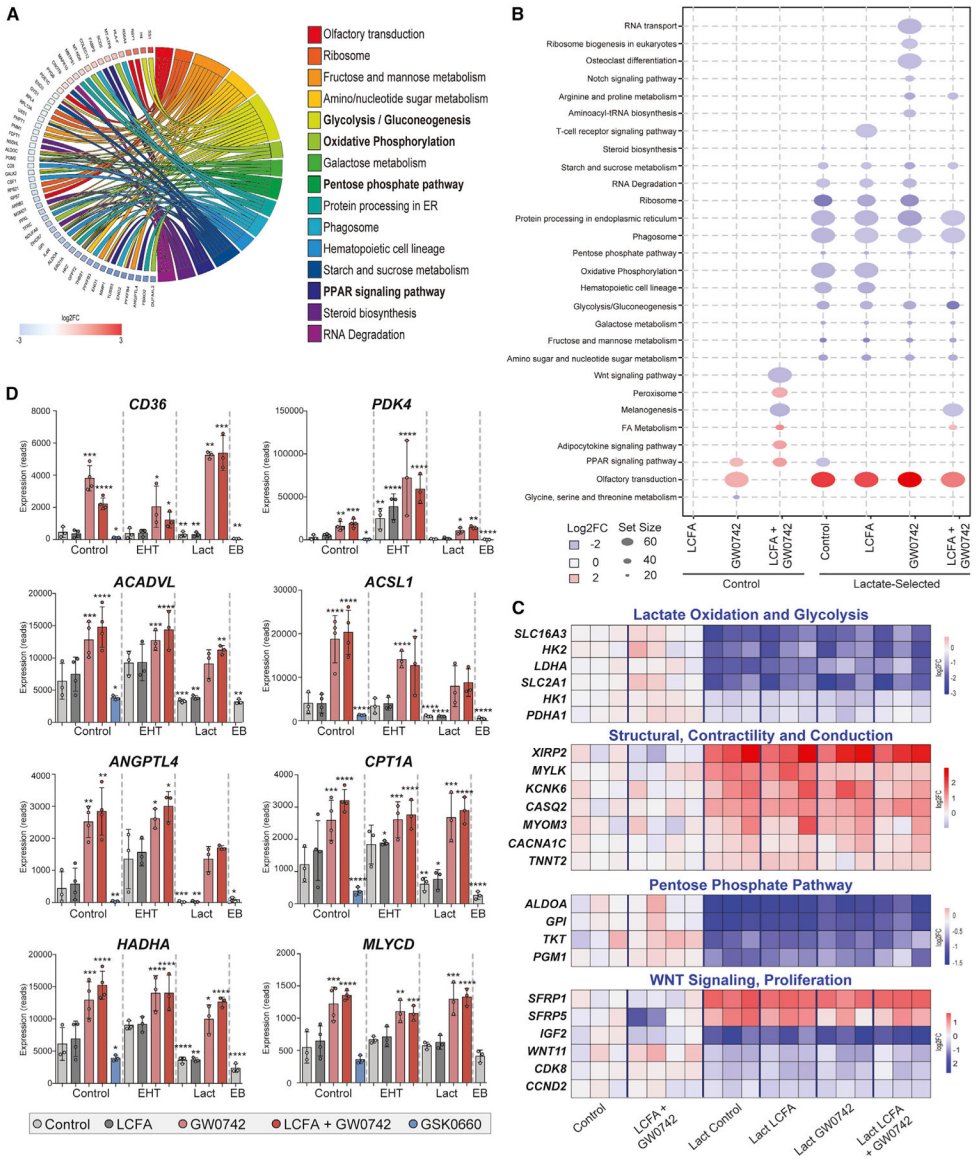

Figure 7. Transient lactate exposure has long-term effects on hPSC-CMs and PPARd activation induces a metabolic switch across multiple culture systems

(A) Chord-plot illustration of differentially regulated KEGG pathways in hPSC-CMs transiently exposed to lactate compared with control.

(B) KEGG pathways comparison between hPSC-CMs after lactate selection and 4 weeks of continuous PPARd modulations relative to control.

(C) Gene expression analysis (RNA-seq data, n = 3) in hPSC-CMs transiently exposed to lactate followed by PPARd modulation (4 weeks) and control.

(D) Gene expression analysis (RNA-seq, n = 3) of PPARd-modulated hPSC-CMs from 2D monolayers (control), EHTs, lactate selection, and age-matched embryoid bodies (EBs). All conditions on FACS-isolated hPSC-CMs (SIRPA+CD90−). Data represented as mean ± SD. Statistics: DESeq2 was used to normalize read counts and determine differentially expressed genes with $p < 0.05$ relative to control (far left).

KEY RESOURCES TABLE

REAGENT or RESOURCE	SOURCE	IDENTIFIER
Antibodies		
Anti-α-Actinin (Sarcomeric) antibody, Mouse monoclonal	Sigma Aldrich	A7732
Anti-Cardiac Troponin T antibody	Abcam	Cat# ab45932; RRID:AB_956386
Anti-ACADVL/VLCAD antibody	Abcam	Cat# ab188872
PPARα Antibody (H-2)	Santa Cruz	Cat# sc-398394
PARγ_2 Antibody (A-1)	Santa Cruz	Cat# sc-166731; RRID:AB_2166204
PPAR delta Polyclonal Antibody	Thermo Fisher	PA1-823A
PMP70 ANTIBODY, AF 488	Fisher Scientific	PIPA1650A48
Alexa Fluor® 488 AffiniPure F(ab')$_2$ Fragment Donkey Anti-Rabbit IgG (H+L)	Jackson Immunoresearch	711-546-152
Alexa Fluor® 594 AffiniPure F(ab')$_2$ Fragment Donkey Anti-Rabbit IgG (H+L)	Jackson Immunoresearch	711-586-152
Alexa Fluor® 647 AffiniPure F(ab')$_2$ Fragment Donkey Anti-Rabbit IgG (H+L)	Jackson Immunoresearch	711-606-152
Alexa Fluor® 488 AffiniPure F(ab')$_2$ Fragment Donkey Anti-Mouse IgG (H+L)	Jackson Immunoresearch	715-546-151
Alexa Fluor® 647 AffiniPure F(ab')$_2$ Fragment Donkey Anti-Mouse IgG (H+L)	Jackson Immunoresearch	715-606-151
Invitrogen™ MitoTracker™ Deep Red FM	Fisher Scientific	M22426
APC anti-human CD172a/b (SIRPα/β) Antibody	Biolegend	323808
PE anti-human CD90 (Thy1) Antibody	Biolegend	328110
APC anti-human CD36 Antibody	Biolegend	336208
Biological samples		
Non-anomalous, de-identified human fetal heart tissue	Icahn School of Medicine at Mount Sinai Biorepository and Pathology Core	N/A
Chemicals, peptides, and recombinant proteins		
DMEM (500 mL)	Life Technologies	11965-118
IMDM	Life Technologies	12440-053
DMEM/F12	Life Technologies	11330057
Penicillin/Streptomycin (100x)	Life Technologies	15140-122
L-Glutamine (200 mM)	Life Technologies	25030-081
EDTA	Corning	46-034-CI
TrypLE Express (1X)	Life Technologies	12605010
Matrigel	Corning	254248
Dulbecco's phosphate-buffered saline (DPBS)	Life Technologies	14190-136
Thiazovivin	Millipore	420220
Stabilized AA	Sigma-Aldrich	A8960
Transferrin	Sigma-Aldrich	10652202001
Sodium Selenite	Sigma-Aldrich	S5261

REAGENT or RESOURCE	SOURCE	IDENTIFIER
bFGF	R&D	233-FB-001MG/CF
Insulin	Sigma-Aldrich	I9278
TGFβ1	R&D	240-B-010/CF
Sodium Bicarbonate	Thermo Fisher Scientific	25080094
NaCl	Sigma-Aldrich	S7653
DMEM (500 mL)	Life Technologies	11965-118
IMDM	Life Technologies	12440-053
DMEM/F12	Life Technologies	11330057
Penicillin/Streptomycin (100x)	Life Technologies	15140-122
L-Glutamine (200 mM)	Life Technologies	25030-081
EDTA	Corning	46-034-CI
TrypLE Express (1X)	Life Technologies	12605010
Matrigel	Corning	254248
Dulbecco’s phosphate-buffered saline (DPBS)	Life Technologies	14190-136
Thiazovivin	Millipore	420220
Stabilized AA	Sigma-Aldrich	A8960
Transferrin	Sigma-Aldrich	10652202001
Sodium Selenite	Sigma-Aldrich	S5261
bFGF	R&D	233-FB-001MG/CF
Insulin	Sigma-Aldrich	I9278
TGFβ1	R&D	240-B-010/CF
Sodium Bicarbonate	Thermo Fisher Scientific	25080094
NaCl	Sigma-Aldrich	S7653
DMEM (500 mL)	Life Technologies	11965-118
IMDM	Life Technologies	12440-053
DMEM/F12	Life Technologies	11330057
Penicillin/Streptomycin (100x)	Life Technologies	15140-122
L-Glutamine (200 mM)	Life Technologies	25030-081
EDTA	Corning	46-034-CI
TrypLE Express (1X)	Life Technologies	12605010
Matrigel	Corning	254248
Dulbecco’s phosphate-buffered saline (DPBS)	Life Technologies	14190-136
Thiazovivin	Millipore	420220
Stabilized AA	Sigma-Aldrich	A8960
Transferrin	Sigma-Aldrich	10652202001
Sodium Selenite	Sigma-Aldrich	S5261
bFGF	R&D	233-FB-001MG/CF
Insulin	Sigma-Aldrich	I9278
TGFβ1	R&D	240-B-010/CF
Sodium Bicarbonate	Thermo Fisher Scientific	25080094
NaCl	Sigma-Aldrich	S7653
BSA	Life tech	15260037

REAGENT or RESOURCE	SOURCE	IDENTIFIER
RPMI	Life Technologies	11875-093
B27+insulin	Life Technologies	17504044
Ascorbic acid	Sigma-Aldrich	A4544
MTG	Sigma-Aldrich	M6145
Lactate	Sigma-Aldrich	L7022
Na-Hepes	RPI	H75050-100.0
Collagenase B	Roche	11 088 831001
Collagenase type 2	Worthington	LS004176
BMP4 (rh)	R&D Systems	314-BP
ActivinA	R&D Systems	338-AC-050
XAV939	Stemgent	04-0046
VEGF	R&D Systems	293-VE
RPMI (-glucose)	Life Technologies	11879020
WY14643	Sigma-Aldrich	Cat#: C7081
GW0742	Sigma-Aldrich	G3295
Rosiglitazone	Sigma-Aldrich	R2408
GW6471	Sigma-Aldrich	G5045
GSK0660	Sigma-Aldrich	G5797
GW9662	Sigma-Aldrich	M6191
Palmitic Acid	Sigma-Aldrich	P0500
Oleic Acid	Sigma-Aldrich	O1008
Linoleic Acid	Sigma-Aldrich	L1376
Bovine Serum Albumin	Sigma-Aldrich	A8806
Fibrinogen	Sigma-Aldrich	F8630
Thrombin from bovine plasma	Sigma-Aldrich	T7513-250UN
Aprotinin from bovine lung	Sigma-Aldrich	A1153
Saponin	Sigma-Aldrich	84510
Propyl gallate	Sigma-Aldrich	P3130
Nail Polish	VWR	100491-940
DAPI (4’,6-Diamidino-2-Phenylindole, Dilactate)	Biolegend	422801
Paraformaldehyde Aqueous Solution, EM Grade,	Electron Microscopy Sciences	15710
Critical commercial assays		
Click-iT Plus EdU Alexa Fluor 488 kit	Life Technologies	C10632
Zymo Research Quick RNA Micro kit	VWR	76020-388
qScript cDNA SuperMix	VWR	101414-108=
XF Cell Mito Stress Test	Agilent	103015-100
Deposited data		
Raw and Analyzed RNASeq data	This paper	GEO: GSE160987
Raw and Analyzed ATACSeq data	This paper	GEO: GSE178984
Experimental models: Cell lines		

REAGENT or RESOURCE	SOURCE	IDENTIFIER
Human: MSN02-4	LINCS Consortium, Icahn School of Medicine at Mount Sinai	N/A
Human: H9 ES Cells	WiCell	WA09
Human: H7 ES Cells	WiCell	WA07
Human: MEL2	WiCell	N/A
Oligonucleotides		
Primer: human PPAR alpha Forward: CGTCCTGGCCTTCTAAACGTA	This paper	N/A
Primer: human PPAR alpha Reverse: AGATATCGTCCGGGTGGTTG	This paper	N/A
Primer: human PPAR delta Forward: GCCCAGTACCTCTTCCCCAA	This paper	N/A
Primer: human PPAR delta Reverse: TTTCGGTCTTCTTGATCCGCT	This paper	N/A
Primer: human PPAR gamma Forward: CGCCCAGGTTTGCTGAATGT	This paper	N/A
Primer: human PPAR gamma Reverse: CTCAGGGTGGTTCAGCTTCA	This paper	N/A
Software and algorithms		
Fiji	Schindelin et al., 2012	https://imagej.net/Fiji/Downloads
flowJo	FLOWJO LLC	https://www.flowjo.com/
MatFiber	Fomovsky and Holmes, 2010	N/A
MatLab	The Mathworks Inc.	https://www.mathworks.com/products/matlab.html
GraphPad Prism 5.0	GraphPad Software Inc.	http://www.graphpad.com/scientific-software/prism/
Kallisto	Bray et al., 2016	N/A
DESeq2	Bioconductor	
R	https://cran.r-project.org/	N/A
UpsetR Plots	Lex et al., 2014	N/A
Axion Integrated Studio (AxIS)	Axion Biosystems	https://www.axionbiosystems.com/resources/product-brochure/axis-brochure
GAGE	Bioconductor	https://bioconductor.org/packages/release/bioc/html/gage.html
Zeiss ZEN 2009	Zeiss	N/A
LabVIEW	National Instruments	https://www.ni.com/en-us/shop/labview.html
Other		
RNASeq Resource Website	This paper	amp.pharm.mssm.edu/dubois/